

Design and Development of a Bat-Inspired Micro UAV

Senior Design Project Report

BY

Ali Haseeb Jaffri 2017062

Minahill Tariq 2017203

Mohammad Hamza Amjad 2017209

Sheikh Abdul Majid 2017437

Supervised by

Dr. Muhammad Ilyas



Faculty of Mechanical Engineering

GIK Institute of Engineering Sciences & Technology

May 2021

ABSTRACT

The increase in frequency of disasters, both natural and man-made, has imposed a huge risk to human life due to the extreme environment surrounding the disaster affected areas. Hence, there is an immediate need to design unmanned vehicles that can assist the rescue team in surveillance and recovery operations. The project focuses on the design of a bat inspired, micro unmanned aerial vehicle, that will be used for disaster management. Several mechanisms, including the watts six bar linkage and crank-shaft, have been installed which allows the machine to exhibit flapping, mediolateral and dorsoventral motions, thus allowing it to achieve all the key degrees of actuation, which significantly contribute to bat flight. The geometric and aerodynamic parameters, having similar values as for the biological bat, have been utilized in the design, which makes the machine highly efficient due to increase in lift and flight range. The structure of the micro-UAV has been modelled on different simulation software, including SolidWorks and MSC Adams, and has been analyzed through the inverse dynamics approach. After performing a detailed kinematic analysis, a mathematical modelling, for the optimization of aerodynamic parameters of the micro-UAV, was developed in order to obtain the synchronicity between the forelimb mechanisms. Moreover, piezo-electric transducers have been installed underneath the elastic wing membrane of the robot, which continuously harvest energy during the flight, hence ensuring minimum energy conservation and maximum flight efficiency. As the machine follows bat morphology, this makes it high maneuverable, thus allowing it to enter narrow and dangerous zones, and ensuring safety for the rescue team during disaster management.

Keywords: micro-UAV, bat-inspired, flapping, silicon membrane, disaster management

Table of Contents

ABSTRACT	i
TABLE OF CONTENTS	ii
NOMENCLATURE	v
LIST OF FIGURES	vi
LIST OF TABLES	vii
 Chapter 1	
INTRODUCTION	1
1.1 Background and Motivation	1
1.2 Problem Statement	1
1.3 Scope of the Work and Expected Outcomes	2
1.4 Report Outline	2
1.5 Project Schedule/Timeline	2
1.6 Individual and Team Contribution	3
 Chapter 2	
LITERATURE REVIEW.....	4
2.1 Literature Review	4
2.1.1 Disaster Robotics.....	4
2.1.2 Natural Flyers	4
2.1.3 Bat Flight	5
2.1.4 Selection Criteria for Bat Species	5
2.1.5 Existing Models	6
2.1.6 Energy Harvesters	7
2.2 Inferences Drawn out of Literature	8

	2.3 Summary	9
Chapter 3	DESIGN AND ANALYSIS.....	10
	3.1 Design Methodology	10
	3.1.1 Selected Forelimb and Hindlimb Mechanism	11
	3.1.2 Selected Flapping Mechanism.....	11
	3.1.3 Actuation.....	12
	3.1.4 Wing Membrane	13
	3.1.5 Design Process Flowchart.....	13
	3.2 Governing Equations/Mathematical Modelling	15
	3.2.1 Governing Equations	15
	3.2.2 Mathematical Modelling for the Optimization of Flapping Frequency.....	21
	3.3 Geometric Modeling and Design	25
	3.4 Analysis.....	27
	3.5 Summary	35
Chapter 4	PHYSICAL MODEL DEVELOPMENT AND TESTING.....	36
	4.1 Development Process	36
	4.1.1 Membrane	36
	4.1.2 Skeleton	38
	4.1.3 Joints	38
	4.1.4 Body	39
	4.1.5 Assembly	39
	4.2 Integration and Instrumentation.....	40
	4.3 Testing/Experimental Procedures.....	43

	4.4 Summary	43
Chapter 5	RESULTS AND DISCUSSION.....	45
	5.1 Results	45
	5.2 Analysis and Discussion	47
	5.2.1 Energy Harvesting	47
	5.2.2 Trajectory Planning	48
	5.2.3 Mathematical Model for Flapping	50
	5.2.4 Pulse Width Modulation Signal Generation	55
	5.3 Summary	60
Chapter 6	IMPACT AND ECONOMIC ANALYSIS	61
	6.1 Social Impact	61
	6.2 Sustainability Analysis	61
	6.2.1 Economics of Project	61
	6.2.2 Scope of Implementation	62
	6.3 Environmental Impact	62
	6.4 Sustainable Development Goals (SDGs)	63
	6.5 Hazard Identification and Safety Measures	64
	6.6 Summary	65
Chapter 7	CONCLUSION AND FUTURE RECOMMENDATIONS.....	66
	7.1 Conclusions	66
	7.2 Future Recommendations	67

REFERENCES	69
APPENDIX A	71
APPENDIX B	76
APPENDIX C	80

Nomenclature

α	Angular acceleration	ρ_{air}	Density of air
α_k	Elemental angle of attack	p_x, p_y, p_z	Center of mass coordinates
AR	Aspect ratio	\mathbf{q}	Parameter vector
b	Wing span	q_a, q_p	Active and passive joints
C_d	Coefficient of drag	$Q_{\vec{F}}$	Generalized Forces
C_k	Elemental chord length	q_x, q_y, q_z	Euler angles of pitch, yaw, roll
C_l	Coefficient of lift	S	Wing area
C_m	Coefficient of moment	SMA	Shape memory alloy
DoA	Degree of actuation	t	Time period
DoF	Degree of freedom	θ	Angular position
DoU	Degree of underactuation	UAV	Unmanned aerial vehicle
e	Train ratio	V	Translational velocity
I	Moment of inertia	ω	Angular velocity
M	Mobility		
m_t	Total mass		
MAV	Micro aerial vehicle		
n	Speed of gear (RPM)		

List of Figures

Figure 1- 1: Project Timeline

Figure 2- 1: Caltech's BatBot, B2

Figure 2- 2: Politecnica's BaTBoT

Figure 2- 3: B2's Forelimb Mechanism

Figure 3- 1: Modularity Flowchart

Figure 3- 2: Design Process Flowchart

Figure 3- 3: Watt's Six Bar Linkage [15]

Figure 3- 4: Articulated Robot Bat Wing [17]

Figure 3- 5: CAD Model of Robot

Figure 3- 6: Model Divisions - forelimbs (red), hindlimbs (blue), body (yellow). All dimensions in mm

Figure 3- 7: Forelimb Model - wrist (red), elbow (blue), shoulder (yellow). All dimensions in mm

Figure 3- 8: Forelimb Mechanism (front view)

Figure 3- 9: Forelimb Mechanism (isometric view)

Figure 3- 10: Translational Displacement of CoM of Finger

Figure 3- 11: Translational Velocity of CoM of Finger

Figure 3- 12: Translational Acceleration of CoM of Finger

Figure 3- 13: Translational Displacement of Slider

Figure 3- 14: Translational Velocity of Slider

Figure 3- 15: Translational Acceleration of Slider

Figure 3- 16: Flapping Mechanism (front view)

Figure 3- 17: Flapping Mechanism (isometric view)

Figure 3- 18: Angular Velocity of Connecting Rod

Figure 3- 19: Membrane Shape

Figure 4- 1: Membrane Manufacturing

Figure 4- 2: Manufactured Membrane

Figure 4- 3: Hollow Carbon Fiber Rods

Figure 4- 4: Manufactured Joints (left to right) - wrist, auxiliary wrist, auxiliary wrist/shoulder, elbow

Figure 4- 5: Wood Router for cutting body slots

Figure 4- 6: Wing Assembly

Figure 4- 7: Flapping Assembly

Figure 4- 8: Gear and Motor Coupling

Figure 4- 9: Flapping Mechanism Body Slot

Figure 4- 10: Skeleton Assembly

Figure 4- 11: Membrane and Piezoelectric Sensor

Figure 5- 1: Piezoelectric Transducer placement

Figure 5- 2: Oscilloscope Waveform

Figure 5- 3: Non-inverting Amplification Circuit

Figure 5- 4: Amplified Waveform

Figure 5- 5: Axes Placement

Figure 5- 6: Initial (left) and Final (right) Position

Figure 5- 7: Electro-mechanical model of motor

Figure 5- 8: PID Control Loop

Figure 5- 9: Autotune Response

Figure 5- 10: Initial Ladder Logic Diagram

Figure 5- 11: Output Configuration

Figure 5- 12: Divide components

Figure 5- 13: Final Divides

List of Tables

Table 1- 1: Individual Contribution

Table 2- 1: Comparison of Existing Models

Table 3- 1: Morphological Chart

Table 3- 2: Geometric Parameters

Table 3- 3: Aerodynamic Parameters

Table 3- 4: Caltech and GIK Model Comparison

Table 3- 5: Caltech and GIK Model Comparison

Table 3- 6: Approximate and Exact Dimensions of Membrane

Table 4- 1: Dragon Skin 10 Medium Properties

Table 5- 1: Waveform Parameters

Table 5- 2: Amplification and Rectification Results [19]

Table 5- 3: DH Table

Table 5- 4: Translational Parameters

Table 5- 5: CL System Response Characteristics

Table 5- 6: Position and State Findings for $t < 2.5s$

Table 5- 7: Position and State Finding for $t > 2.5s$

Table 6- 1: Bill of Materials

Table 6- 2: SDG Mapping

Chapter 1

INTRODUCTION

1.1 Background and Motivation

Due to increasing climatic changes, frequency of disasters has also increased. This consequently increases the risk to human lives, especially rescue workers. Often times, disaster affected areas exhibit extreme environments, such as fire outbreak, chemical leakage and nuclear radiation, where it is not feasible for a rescue worker to enter [1].

Unmanned Air Vehicles (UAV) such as conventional drones could be used in such situations but they have fixed dimensions and cannot move through tight spaces, contain sharp propellers that could be hazardous to people being rescued in case of malfunction and cannot be operated under extreme weather conditions. A micro-UAV that can access tight spaces and exhibits agility and maneuverability will be much suited for this application.

Taking inspiration from nature has been the norm for numerous inventions. Although the complexity of motion and material properties may often be impossible to replicate, the approach itself significantly optimizes the design process. Owing to the bat's complex wing motion, it can perform several agile maneuvers in small spaces with ease. Thus, it poses as an attractive source of inspiration for a potential aerial robot.

1.2 Problem Statement

Disaster-affected areas tend to exhibit extreme environments, such as fire outbreak, chemical leakage and nuclear radiation, where it is not feasible for a rescue worker to enter, thus creating a need for robots to act as surrogates to rescue workers. By taking inspiration from nature, design and develop an autonomous flying machine having morphology similar to that of a bat to assist in reconnaissance and surveillance operations in the event of a disaster.

1.3 Scope of the Work and Expected Outcomes

The aim of this project is to design and develop a bat-inspired micro-UAV. The scope of this includes following objectives:

- To design and analyze the feasibility of bat-like robot
- To simulate the design using modern computational tools
- To fabricate and assemble a prototype using resources available at the GIK Institute
- To autonomously execute point-to-point flight
- To test the machine under various simulated conditions of disaster

Once all the objectives are completed, a bat-inspired micro-UAV will be achieved that will not only replicate the maneuvers in a flight of a biological bat, but the micro-UAV will also be able to fly autonomously on a pre-defined path that will eventually help the rescue workers in surveillance and reconnaissance. However, generation of path in real time using machine learning and neural links is out of the scope of this project.

1.4 Report Outline

Chapter 1 – This chapter discusses the background and the motivation to carry out the project, in relation to the problem. Defines the scope of this project and the expected outcomes.

Chapter 2 – This chapters contains the literature survey of the area of study. It discusses the practices and approaches currently being used for similar application. It also provides a comprehensive overview of the research gaps and areas of improvement.

Chapter 3 – This chapter presents the design methodology adopted, governing equations, geometric modelling and design as well as the environmental and social impacts of this project.

Chapter 4 – This chapter presents the step-by-step procedures adopted to carry out fabrication as per the required conditions along with the details regarding instrumentation, testing and experimental procedures.

1.5 Project Schedule/Timeline

Figure 1-1 shows the planned and actual timeline for the project, along with major milestone markers.

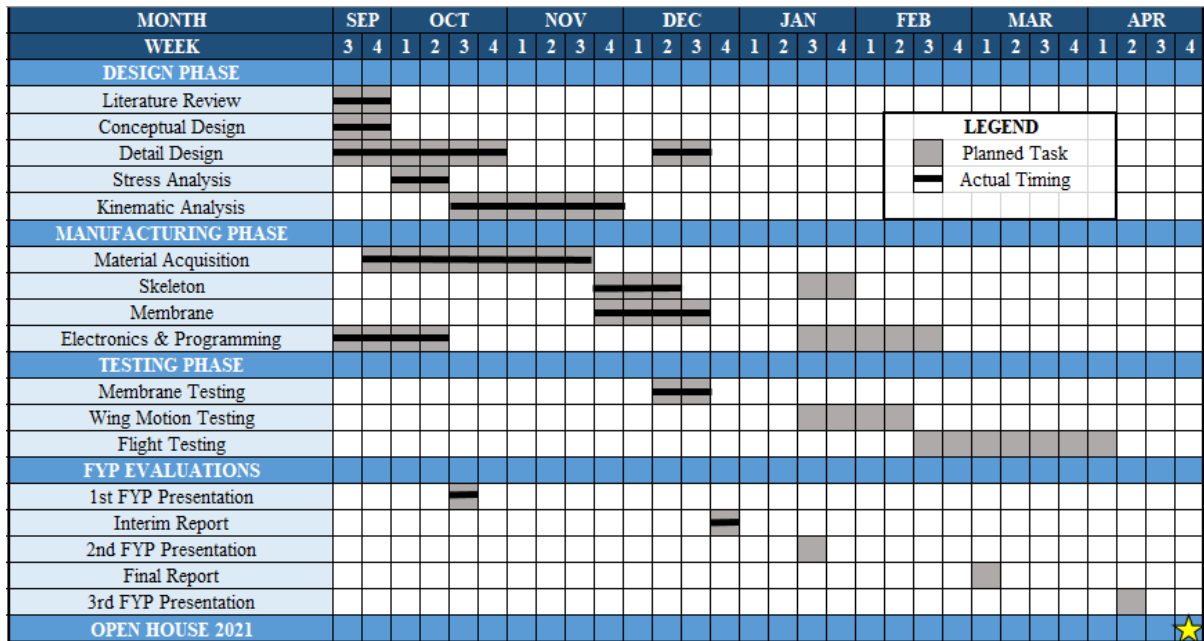


Figure 1- 1: Project Timeline

1.6 Individual and Team Contribution

The teamwork was divided into four main sections, with each group member leading one domain each:

Table 1- 1: Individual Contribution

Member	Domain	Description
Ali Haseeb Jaffri	Electronics	Responsible for the control system and electronic structure of the project
Minahill Tariq	Design and Modelling	Responsible for the CAD modelling and design of project
Mohammad Hamza Amjad	Manufacturing	Responsible for the fabrication and material acquisition of project
Sheikh Abdul Majid	Design Analysis	Responsible for the theoretical analysis of design and simulation of project

As a team, all members contributed towards the making of this report and any further presentations. Each member was head of their domain but provided assistance when and where needed in each domain.

Chapter 2

LITERATURE REVIEW

2.1 Literature Review

2.1.1 Disaster Robotics

Disaster robots aid stakeholders and concerning authorities to tackle the increasing number and complexity of urban catastrophes and life-threatening severe events by providing them the capability of accessing an area of interest. If a disaster has occurred, it may be unbearable, dangerous, or too inefficient for a responder to step into the hot zone in person. On the other hand, robots can penetrate further than the 3 to 4 meters a camera on a wand can extend into densely packed debris. As they do not require food to be brought with them or create bio waste to be disposed of. Most importantly, they are not alive. Likewise, in some missions, such as a chemical or nuclear emergency, the robot is expected to do tasks a person could normally do (e.g., turning a valve) and in environments that a person could normally work in [1].

2.1.2 Natural Flyers

Mechanisms involved in movements of biological species provide critical insights for exploring new technologies and mimicking intelligent systems that are the result of millions of years of evolution [2]. Much effort has been put in recent years in designing biologically inspired micro-robots, commonly known as biomimetic robots, especially flapping robots as they can exhibit agility and maneuverability almost similar to their biological equals [3] [4]. There is an overwhelming variety of flying animals found in nature to take inspiration from, ranging from as small as mosquitoes to as large as flying foxes. Regardless of the size, they all utilize similar mechanisms to flap their wings. Slight differences in their mechanisms and flying patterns may be due to the environment of each flying species [5]. Amongst these flying animals, bats have long been a topic of interest because of their unrivaled agility and mid-air maneuvering capabilities. Thus, making them a perfect example to replicate and implement in applications such as surveillance and rescue missions.

2.1.3 Bat Flight

Bats incorporate the most sophisticated mechanism in their flight [3]. This is achieved with the help of 40 active and passive Degrees of Freedom (DoF). Muscles and bones are connected via different interlocking joints, such as ball and socket and revolute that interlock, creating a musculoskeletal structure that also helps bat move in multiple independent directions [6].

In general, one wingbeat cycle involves two independent motions – downstroke movement, in which forelimbs expand backwards while simultaneously sweeping downwards and forward with respect to central body, and the upstroke movement, in which forelimbs are brought upwards and backwards while the wings are folded by flexing elbows and wrists [7].

2.1.4 Selection Criteria for Bat Species

To successfully replicate the flight of a biological bat, several parameters, such as weight, wingspan and wingbeat frequency are needed to be taken into consideration. There are estimated to be over 1400 species of bat with their wingspan ranging from 0.15m for “*Craseonycteris thonglongyai*” micro bat to 1.82m for “*Pteropus vampyrus*” mega bat. Likewise, their mass ranges from 2g to 1kg respectively [5]. Wingbeat frequency for bats, like any flapping mechanism, depends on weight and wingspan. For a body mass of 2g, the wingbeat frequency of a bat is 16 Hz. Similarly, for a body mass of 1 kg, frequency reduces to 3.1 Hz [8].

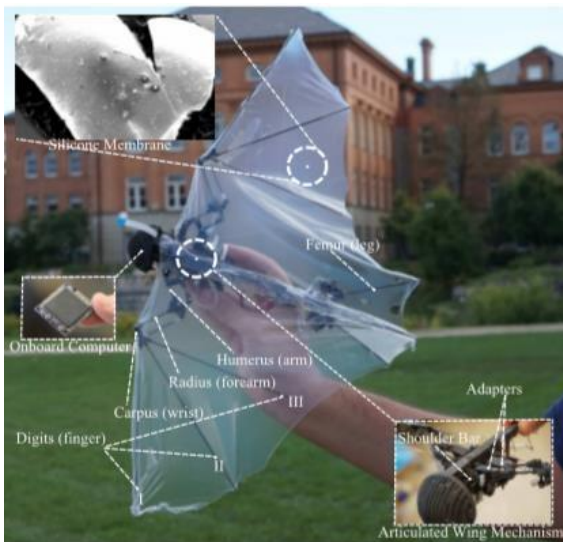


Figure 2- 1: Caltech's BatBot, B2 [3]

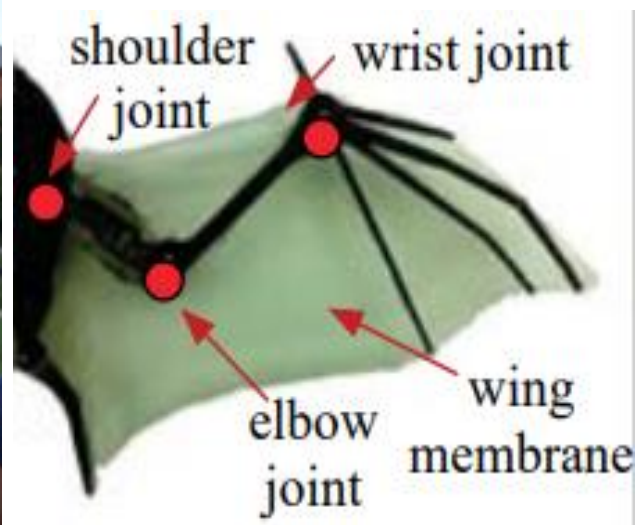


Figure 2- 2: Politecnica's BatBoT [5]

Major structural components in B2 consist of arm wing, proximal hand wing, distal hand wing, hind limbs and body. The forelimb consists of 12 links made of hollow carbon fiber tubes, providing support for actuators, wherein the distribution of torsional forces across the forelimbs are proportional to the second moment of inertia of the tube cross-section [3]. Each of the forelimbs incorporate the use of Watt's six-bar linkage mechanism with links attached to one another using 1 DoF revolute joints requiring only one



Wing flexibility plays significant role in achieving complex flight maneuvers and high agility as it gives bats shape-changing capabilities. A highly elastic and flexible material is required. After careful examination of anatomical properties of wing membrane of bats, it was found

that weight per unit area, thickness, stretchability and tensile modulus are some of the key features of the membrane [3]. Experiments show that Silicone is more aerodynamically suitable for wing membrane [5]. Both Shape Memory Alloys (SMAs) and microprocessors with sensors can be used to achieve autonomous flight. However, a Lithium polymer (LiPo) battery is utilized to power both types of avionics. Such batteries are often too heavy that an additional lift is needed to be generated to compensate the weight added by batteries and have low storage capacity that they need to be recharged after several hours of operations. An alternate source of energy, that is both light-weight and allows more service hours is, therefore, needed to be utilized in place of a LiPo battery. This can be done by harvesting energy from the vibrations generated by the flapping mechanism of the robot.

Table 2- 1: Comparison of Existing Models

Parameters	Caltech B2 [3]	Politecnica BaTBoT [5]
Weight	93g	125g
Wing Span	46.9cm	46cm
Wing Structure	Carbon Fiber	Carbon Fiber
Wing Membrane	Silicone with platinum catalyst pressed above 10000kg	Smooth-On Dragin Skin series silicon
Body Casing	None	None
Motor	Brushless DC	None
Actuating Power	Crank-shaft mechanism with planetary gearheads	SMA Muscles
Automation	Autonomous	Semi-autonomous
Microprocessor	Custom-built microchip	Arduino Nano

2.1.6 Energy Harvesters

Energy harvesting refers to a process where energy from sources such as vibrations and temperature gradients is harvested and converted to obtain useful electrical energy [9]. This provides an efficient alternative to battery-operated systems, especially where electronics are usually operated at low power levels and self-sustenance is a requirement [10] [11]. Piezoelectricity refers to the electric charge accumulated in certain type of materials when applied with mechanical stresses and vibrations [12]. Piezoelectric materials, when mechanically deformed, produce an alternating current (AC) which can then be scavenged and converted to direct current (DC) to power electronics and sensors. A study conducted to investigate the capability of harvesting energy through a unimorph piezoelectric membrane

transducer found that a 25 mm diameter membrane is capable of generating 1.8 mW with a resonance frequency of 2.58 kHz across a 56 k Ω resistor [13].

The use of piezoelectric materials to harvest energy has already become popular since its early investigation in the late 1990s [14]. DARPA has been funding researches and project to harness energy from blood pressure, leg and arm motions to power implantable and wearing sensors. Piezoelectric materials have also been used to determine the magnitude of impact forces as well as harvesting energy from nano brushes. However, these type of energy harvesters have never been used to power flying robots.

2.2 Inferences Drawn out of Literature

The concept of biologically-inspired bat robot with flapping mechanism possesses several advantages over conventional aerial drones, such as quadcopters. The robot, with its ability to perform complex flight maneuvers, can access locations where movement of conventional drones is limited. While there have been some developments in recent years with regards to bio-inspired robots, replicating a bat's flight is still a challenging concept. The complexities involved in wing kinematics and flexibilities pose number of technological challenges in modelling and controlling robot. Due to this, the two models referenced in literature have only been able to achieve autonomous flight for shorter distances.

Caltech's B2 provides a skeletal structure that can be replicated at this level with technologies and material available in Pakistan. A noticeable gap found in research is the limited application of energy harvesters to power unmanned vehicles. Since the electronics and sensors used to achieve autonomous flight operate at low voltages and powers and batteries tend to be much heavier than the robots itself, use of energy harvesters such as piezoelectric transducers would significantly reduce the overall weight. This project will intend to reduce this gap by testing the feasibility of piezoelectric transducers to achieve self-sustained autonomous flight while also modifying the design and electronics to increase the range of and number of movements performed by the robot.

2.3 Summary

This chapter presents a comprehensive review on biologically-inspired bat robots. A specialized literature survey from [5] and [3] provides critical insights on selection criteria for species and material for the robot with a special emphasis on its application in disaster management. The literature survey also provides information regarding the potential use of piezoelectric transducers to power the robot in order to reduce its overall weight.

Chapter 3

DESIGN AND ANALYSIS

3.1 Design Methodology

The design of a micro unmanned aerial vehicle consists of complex mechanisms, each of which is dedicated to achieve one of the key degrees of actuations. For a UAV having bat morphology, the key DOAs are forelimb flapping motion, forelimb folding and unfolding motion and hindlimb upward and downward motion. In order to achieve all the essential motions required for a bat flight, the alternatives for each motion were selected from the available literature of UAVs having bat morphology. A morphological chart, shown in Table 3-1 was then formed to ensure the selection of the most optimum mechanisms against each key DOA. The chart not only compares the mechanisms, but also proposes the actuation methods for different mechanisms. Moreover, the alternatives for the wing membrane have also been listed down.

Table 3- 1: Morphological Chart

Sub-problem Solution Concepts				
Actuation	Forelimb mechanism	Hindlimb mechanism	Flapping mechanism	Wing membrane
Combination of planetary gearheads and spindle drives	Watt's six bar chain mechanism	Leg, actuation bar and control rod linkage	1 DoF adapters attached at shoulder links	Vulcanized silicone at 10,000 kg with platinum catalyst
Crank rocker mechanism with angular gear unit	Links based on scissor kinematics	SMA-actuated hindlimbs	Rack and pinion gear unit	Knitted elastane fabric with 45,000 spot-welded polyethylene film
Short strips of shape memory alloys (SMA) functioning as muscles	Singular links joined with SMA muscles	Absence of hindlimbs	Geared down transmission system	Commercial silicon elastomers

3.1.1 Forelimb and Hindlimb Mechanism

The selected mechanism for the forelimb mechanism is a Watts Six bar chain which has been modified by the addition of a link connecting the humeral and humeral support links, and the by the replacement of the revolute joints by ball and socket joints at the two ends of the radial support link. The mechanism was preferred because of its cost effectiveness as compare to the other two. Also, the response of watts six-bar chain to the changes in folding and unfolding of the wings will be faster as compared to the shape memory alloys. Lastly, for the hindlimb mechanism, a 3-bar linkage composing of the leg, an actuation bar, and a control rod was selected.

3.1.2 Flapping Mechanism

The selected mechanism for achieving the flapping motion is the crank shaft mechanism. The motor connected in the fuselage will be geared down to rotate the crank which in turn rotate

the adapters connecting the shoulder and humeral and humeral support links. The mechanism was preferred over rack and pinion because of its less complex analysis and cost-effectiveness (gears would cost more than simple carbon fiber links).

3.1.3 Actuation

The actuating mechanism selected for the forelimb mechanism is a one degree of freedom spindle drive which will be connected to the planetary gear head, used to gear down the DC motor. On the other hand, for the hindlimb actuation, linear motion is achieved through the use of a lead screw. Lastly, for the flapping mechanism, a spur gear train is used to gear down the RPM of the DC motor, which is then connected to the cranks on both sides of the fuselage to achieve synchronous motion. The entire motion is controlled by a Raspberry Pi controller supplemented with a Pixhawk Flight controller via Micro Air Vehicle Link (MAVLink) protocol for real-time communication. An Xbox Kinect Sensor is used to map the testing environment and a Global Navigation Satellite System (GNSS) module is used for navigation. The Inertial Measurement Unit (IMU) is used to measure angular rate, orientation and specific force of the robot by using the combination of gyroscope and accelerometer. In order to investigate the feasibility of powering the robot using piezoelectric energy harvester, the on-board battery is supplemented with an energy harvester. A modularity chart of the electronic system for the robot is shown in the Figure 3-1.

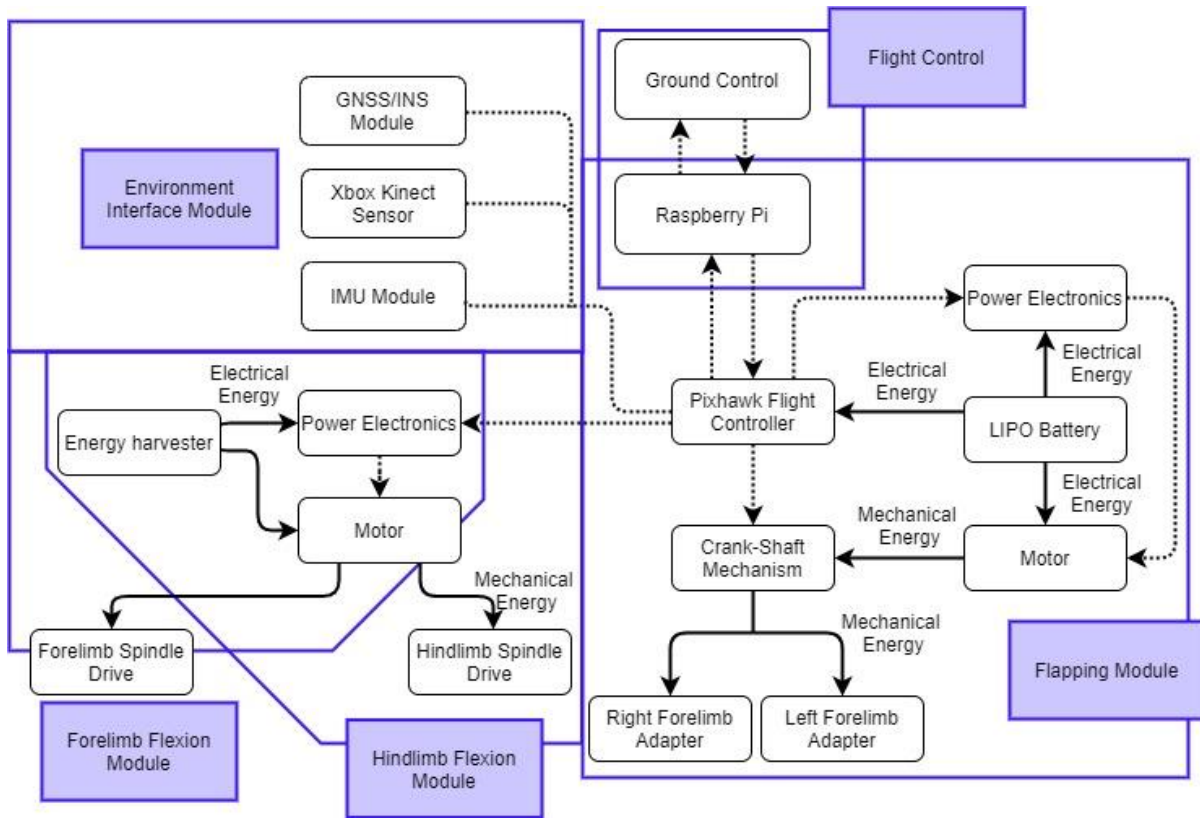


Figure 3- 1: Modularity Flowchart

3.1.4 Wing Membrane

For the membrane, Smooth-On Dragon Skin Series [15] silicon has been used which was cured after pressing between two glass sheets, to obtain the desired membrane properties. The other alternatives were rejected because of their high cost due to the presence of platinum as well as having elastic properties are not comparatively better than silicone.

3.1.5 Design Process Flowchart

The procedure to be followed in the design and development of the micro-UAV has been summarized in the form of a flow chart in Figure 3-2.

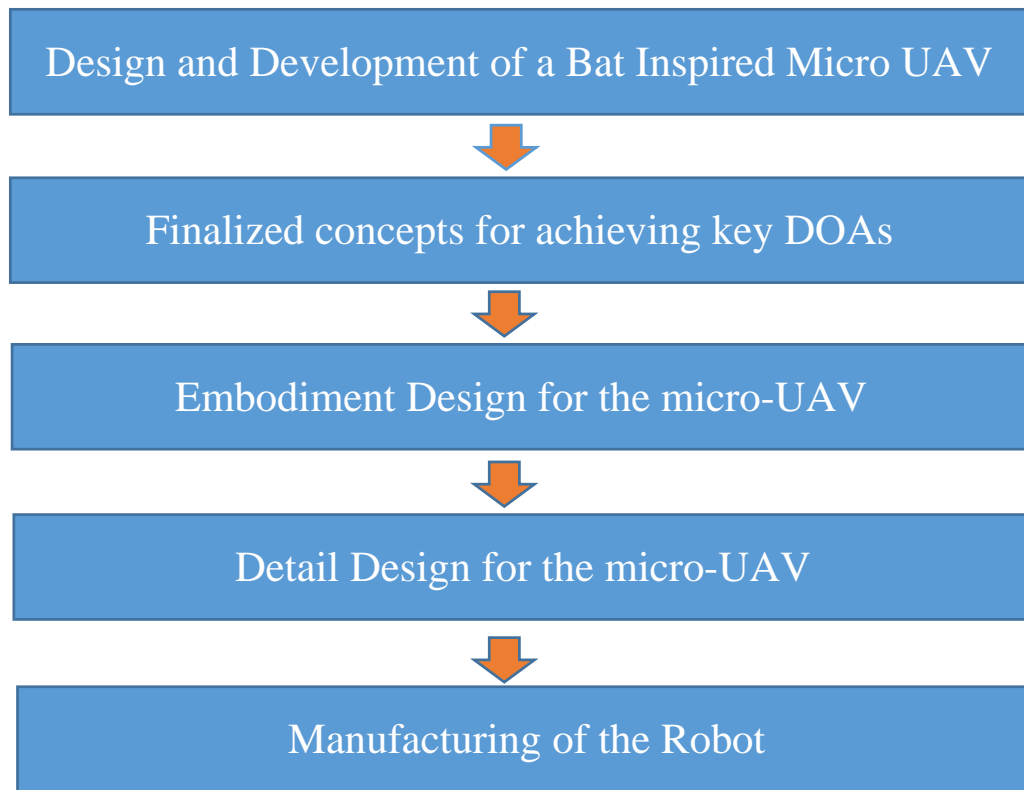


Figure 3- 2: Design Process Flowchart

After the problem identification, the team entered the conceptual design phase, in which the mechanisms for forelimb, hindlimb and flapping were finalized in order to achieve the five key degrees of actuation. The concepts were generated by utilizing the approach of morphological charts, in which the functions and sub-functions were arranged in a logical order, and a feasible combination of concepts was made. After finalizing the concepts, the team entered in the embodiment design phase in which the layouts were made for different parts of the robot. Here, the components were clustered in to modules and interactions between different modules were identified. Moreover, the material for the links and membrane was also finalized through systematic techniques such as Ashby charts. Finally, the manufacturing processes were identified for the fabrication of the robot.

Currently, the team is working under the detail design and manufacturing phase; the dimensions for the forelimb mechanism have been finalized and the exact dimensions for the gears to be used in flapping and actuation, are being determined. While the membrane and

joints for the forelimb mechanism have been manufactured, the team is finalizing the overall dimensions of the robot, in order to completely wrap up the detail design phase.

3.2 Governing Equations/Mathematical Modelling

The inverse dynamics approach has been adopted for the kinematics and dynamics analysis of the micro-UAV. However, for the calculation of initial kinematic parameters, some correlations, found from literature have been used. Then the initial parameters were used to build the overall structure of the robot on which the inverse dynamics approach will be implemented.

In addition, the Lagrangian method is adopted for the optimization of the flapping frequency of the robot. The mathematical modeling, shown in this section, will be used to solve the non-linear differential equations, which will provide us the optimized aerodynamic parameters.

3.2.1 Governing Equations

The first step in the analysis of the design is the determination of geometric parameters of the micro-UAV. Keeping in view the resources and availability of material, the team decided to constraint the weight to a maximum of 500g. After deciding the weight, the scaling factors/correlations of the geometric parameters for the same species (*Rousettus aegyptiacus*) of the bat, which we are designing, was found from the literature [16]. Table 3-2 summarizes the scaling factors for different kinematic parameters related to the geometry of the bat, and also shows their corresponding values when mass, m_t , was input as 500g.

Table 3- 2: Geometric Parameters

Parameter	Scaling Factor	Value
Minimum Wingspan, b_{min}	$m_t^{0.423}$	0.746m
Maximum Wingspan, b_{max}	$m_t^{0.366}$	0.776m
Maximum Wing Chord, c_{max}	$m_t^{0.357}$	0.781m
Maximum Wing Area, S_{max}	$m_t^{1.32}$	0.401m ²
Wing Loading, Q_s	$m_t^{0.233}$	0.851Nm ⁻²
Aspect Ratio, AR	$m_t^{0.072}$	0.951

Similarly, for the determination of the aerodynamic parameters, the correlations were obtained from the literature [16], consisting of similar designs of bat-inspired micro-UAV. The values of the parameters and their corresponding scaling factors are summarized in Table 3-3.

Table 3- 3: Aerodynamic Parameters

Parameters	Scaling Factor	Value
Minimum Wingbeat Period, T	$m_t^{0.18}$	0.883s
Downstroke Duration, T_{down}	$m_t^{0.213}$	0.863s
Downstroke Ratio, τ_{down}	$m_t^{0.036}$	0.975
Maximum Wing Stroke Amplitude, ϕ_s	$\log(m_t)(-3.058)$	52.744°
Strouhal Number, St	$m_t^{-0.088}$	1.063
Minimum Angle of Attack, α	$\log(m_t)(-7.738)$	2.329°
Wing Camber at Maximum Span	$m_t^{0.9}$	0.536
Minimum Lift Coefficient, C_L	$m_t^{0.17}$	0.889

After the determination of the geometric and aerodynamic parameters, the team proceeded towards the inverse dynamics approach. The maximum wingspan obtained from the scaling factors is 0.746m. Based on the calculated wingspan, the modified watts six-bar linkage

(forelimb mechanism) was designed on MSC Adams. Following equations were used for the analysis of the forelimb mechanism [17]:

$$M = 3(L - 1) - 2J_2 - J_1 \quad (3.1)$$

where M is the mobility or degrees of freedom, L denotes the number of links, J_1 denotes the number of 1 DOF (full) joints and J_2 denotes the number of 2 DOF (half) joints, and:

$$I = \frac{m(3a^2 + 3b^2 + l^2)}{12} \quad (3.2)$$

where I is the moment of inertia along the lateral axis of the cylinder about its center of gravity, a and b are the inner and outer radius respectively, and l is the length of the cylinder

Position Analysis:

The watts six-bar linkage can be treated as a series of connection of two four-bar linkages, as shown in Figure 3-3 [17]. Hence, all the relations applicable in the four-bar linkage, have to be applied twice, and the output conditions of the first linkage will be treated as an input for the second linkage.

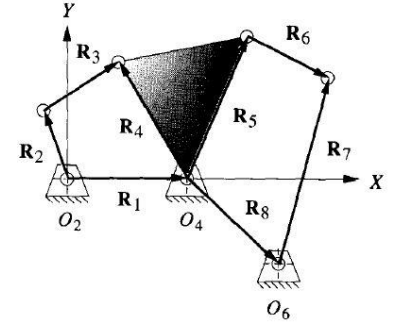


Figure 3- 3: Watt's Six Bar Linkage [17]

Here, only the equations for a single four-bar linkage are shown [17], as they would be the same for both the four-bar linkages connected in series.

$$\theta_{4(1,2)} = 2 \tan^{-1} \left(\frac{-B \pm \sqrt{B^2 - 4AC}}{2A} \right) \quad (3.3a)$$

$$\theta_{3(1,2)} = 2 \tan^{-1} \left(\frac{-E \pm \sqrt{E^2 - 4DF}}{2D} \right) \quad (3.3b)$$

Where θ is the angle between the links relative to the local coordinate system and the constants are defined as follows [17]:

$$A = \cos \theta_2 - K_1 - K_2 \cos \theta_2 + K_3 \quad (3.3c)$$

$$B = -2 \sin \theta_2 \quad (3.3d)$$

$$C = K_1 - (K_2 + 1) \cos \theta_2 + K_3 \quad (3.3e)$$

$$D = \cos \theta_2 - K_1 + K_4 \cos \theta_2 + K_5 \quad (3.3f)$$

$$E = -2 \sin \theta_2 \quad (3.3g)$$

$$F = K_1 + (K_4 - 1) \cos \theta_2 + K_5 \quad (3.3h)$$

$$\text{Where } K_1 = \frac{d}{a}, K_2 = \frac{d}{c}, K_3 = \frac{a^2 - b^2 + c^2 + d^2}{2ac}, K_4 = \frac{d}{b}, \text{ and } K_5 = \frac{c^2 - d^2 - a^2 - b^2}{2ab}$$

Velocity Analysis:

Following equations will be used for the velocity analysis of the forelimb mechanism [17]:

$$V_A = ja\omega_2(\cos \theta_2 + j \sin \theta_2) = a\omega_2(-\sin \theta_2 + j \cos \theta_2) \quad (3.4a)$$

$$V_{BA} = ja\omega_3(\cos \theta_3 + j \sin \theta_3) = a\omega_3(-\sin \theta_3 + j \cos \theta_3) \quad (3.4b)$$

$$V_B = ja\omega_4(\cos \theta_4 + j \sin \theta_4) = a\omega_4(-\sin \theta_4 + j \cos \theta_4) \quad (3.4c)$$

where V is the velocity and A and B are any two points between a link of the watts six bar linkage. The rotational velocities are defined as follows [17]:

$$\omega_3 = \frac{a}{b} \frac{\omega_2 \sin(\theta_4 - \theta_3)}{\sin(\theta_3 - \theta_2)} \quad (3.5a)$$

$$\omega_4 = \frac{a}{b} \frac{\omega_2 \sin(\theta_2 - \theta_3)}{\sin(\theta_4 - \theta_3)} \quad (3.5b)$$

Acceleration Analysis:

After finding the rotational and translational velocities of the links, the acceleration analysis will be done with the help of the following equations [17]:

$$A_A = a\alpha_2(-\sin \theta_2 + j \cos \theta_2) - a\omega_2^2(\cos \theta_2 + j \sin \theta_2) \quad (3.6a)$$

$$A_{BA} = b\alpha_3(-\sin \theta_3 + j \cos \theta_3) - b\omega_3^2(\cos \theta_3 + j \sin \theta_3) \quad (3.6b)$$

$$A_B = c\alpha_4(-\sin \theta_4 + j \cos \theta_4) - c\omega_4^2(\cos \theta_4 + j \sin \theta_4) \quad (3.6c)$$

where A is the acceleration and the subscripts show any two points (A and B) on a link of the watts six bar linkage. The angular accelerations are defined as follows [17]:

$$\alpha_3 = \frac{CD-AF}{AE-BD} \quad (3.7a)$$

$$\alpha_4 = \frac{CE-BF}{AE-BD} \quad (3.7b)$$

where,

$$A = c \sin \theta_4 \quad (3.7c)$$

$$B = b \sin \theta_3 \quad (3.7d)$$

$$C = a\alpha_2 \sin \theta_2 + a\omega_2^2 \cos \theta_2 + b\omega_3^2 \cos \theta_3 - c\omega_4^2 \cos \theta_4 \quad (3.7e)$$

$$D = c \cos \theta_4 \quad (3.7f)$$

$$E = b \cos \theta_3 \quad (3.7g)$$

$$F = a\alpha_2 \cos \theta_2 - a\omega_2^2 \sin \theta_2 - b\omega_3^2 \sin \theta_3 + c\omega_4^2 \sin \theta_4 \quad (3.7h)$$

After finding the accelerations of each link of a watts six bar linkage, the kinematic analysis comes to an end. Now, using the accelerations and inertia properties of the links, the dynamics analysis will be conducted.

Dynamic Analysis:

For the dynamic analysis, we will again divide the watts six bar linkage in to two four bar linkages connected in series. For a single four bar linkage, the total number of unknowns are 9. These unknowns include the reaction forces between the moments, represented by R, the external forces, represented by F and the reaction torque, denoted by T. The unknowns are found with the help of a matrix, shown below [17]:

$$\begin{bmatrix}
1 & 0 & 1 & 0 & 0 & 0 & 0 & 0 & 0 \\
0 & 1 & 0 & 1 & 0 & 0 & 0 & 0 & 0 \\
-R_{12y} & R_{12x} & -R_{32y} & R_{32x} & 0 & 0 & 0 & 0 & 1 \\
0 & 0 & -1 & 0 & 1 & 0 & 0 & 0 & 0 \\
0 & 0 & 0 & -1 & 0 & 1 & 0 & 0 & 0 \\
0 & 0 & R_{23y} & -R_{23x} & -R_{43y} & R_{43x} & 0 & 0 & 0 \\
0 & 0 & 0 & 0 & -1 & 0 & 1 & 0 & 0 \\
0 & 0 & 0 & 0 & 0 & -1 & 0 & 1 & 0 \\
0 & 0 & 0 & 0 & R_{34y} & -R_{34x} & -R_{14y} & R_{14x} & 0
\end{bmatrix} \times \begin{bmatrix} F_{12x} \\ F_{12y} \\ F_{32x} \\ F_{32y} \\ F_{43x} \\ F_{43y} \\ F_{14x} \\ F_{14y} \\ T_{12} \end{bmatrix} = \begin{bmatrix} m_2 a_{G2x} \\ m_2 a_{G2y} \\ I_{G2} \alpha_2 \\ m_3 a_{G3x} - F_{px} \\ m_3 a_{G3y} - F_{py} \\ I_{G3} \alpha_3 - R_{px} F_{py} + R_{py} F_{px} \\ m_4 a_{G4x} \\ m_4 a_{G4y} \\ I_{G4} \alpha_4 - T_4 \end{bmatrix} \quad (3.8)$$

This concludes the dynamic analysis of the forelimb mechanism. Now for the crank shaft mechanism, the same approach can be used, with the slider as the fourth linkage. However, certain restrictions will be imposed in the analysis of flapping mechanism, for example, rotational velocity of the slider will be zero, and this will in fact make the kinematics and eventually the dynamics analysis of the flapping mechanism simpler as compare to that of watts six bar linkage.

Gear Train Formula:

The motor connected in the fuselage has to be geared down in order to achieve the desired RPM required for the flapping mechanism. For this purpose, a gear train is formed with a combination of spur gear and pinion. The gear train also helps in achieving a synchronous motion by powering both the cranks (one on each side of the fuselage) through one source [18].

$$n_L = e * n_F \quad (3.9a)$$

where n_F is the speed of the first gear and n_L is the speed of the last gear and e is the train value defined as:

$$e = \frac{\text{Product of Driving tooth numbers}}{\text{Product of driven tooth numbers}} \quad (3.9b)$$

For a case of a pinion (driving) and a spur gear (driven), the above equation can be written as [18]:

$$n_2 = \frac{N_2}{N_3} n_1 = \frac{d_2}{d_3} n_1 \quad (3.10)$$

where d is the pitch diameter.

3.2.2 Mathematical Modelling for the Optimization of Flapping Frequency

The links and joints of the wings of the robot form an open kinematic chain influenced by gravitational and aerodynamic parameters. The Langrangian method [19], which fundamentally is the difference of the total kinetic potential energies, has been adopted essentially to perform a detailed analysis of the flight and to achieve an

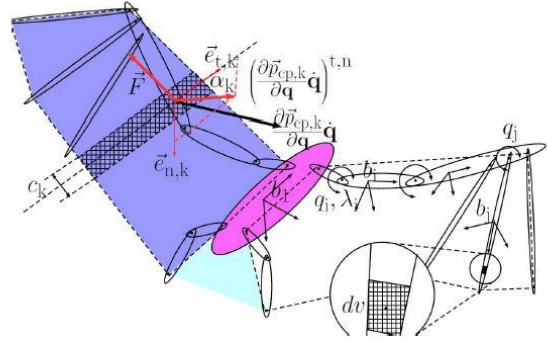


Figure 3- 4: Articulated Robot Bat Wing [19]

optimized value of parameters after fabrication. The open kinematic chain is defined by a configuration variable vector, \mathbf{q} , where $\mathbf{q} = (q_x, q_y, q_z, p_x, p_y, p_z, q_p, q_a)$. In this vector, q_x, q_y, q_z are Euler angles of roll, pitch, and yaw, p_x, p_y, p_z are body center of mass positions and q_a, q_p are spatial positions of active and passive joints respectively.

Figure 3-4 shows that the links of the wings form a shape of a polygon and n is the inertial frame. b_i is the coordinate frame on the center of mass of the i^{th} link. After the transformations and application of Hamilton's principle of least action, the following equation has been obtained [19]:

$$\mathcal{M}(\mathbf{q})\ddot{\mathbf{q}} + \mathcal{C}(\mathbf{q}, \dot{\mathbf{q}})\dot{\mathbf{q}} + \mathcal{G}(\mathbf{q}) = \mathcal{Q} \quad (3.11)$$

For each i^{th} actuated coordinate and the left- or right-wing aerodynamic force, the constraint force adds up to the generalized force. After the application of virtual work, the following equation has been obtained for the generalized forces:

$$Q_\lambda = \left(\frac{\partial q_a}{\partial \mathbf{q}} \right)^T (\lambda_1, \dots, \lambda_i, \dots, \lambda_{m_a})^T \quad (3.12)$$

In order to take in to account the unsteady flow conditions at the separation point, the following ordinary differential equation has been used:

$$\tau_1 \dot{v} + v = v_0 (\alpha_k - \tau_2 \dot{\alpha}_k) \quad (3.13)$$

where v is the position of the separation point and α_k is the elemental angle of attack, given by the formula:

$$\alpha_k = \cos^{-1} \left(\left(\vec{e}_{t,k} \right)^T \frac{\left(\frac{\partial \vec{p}_{cp,k}}{\partial \mathbf{q}} \dot{\mathbf{q}} \right)^{t,n}}{\left\| \left(\frac{\partial \vec{p}_{cp,k}}{\partial \mathbf{q}} \dot{\mathbf{q}} \right)^{t,n} \right\|_2} \right) \quad (3.14)$$

To determine the elemental generalized force, elemental coefficient of lift, $C_{l,k}$, quarter-cord moment, $C_{m,k}$, and elemental drag coefficient, $C_{d,k}$, is also required.

The constants mentioned above can be determined through the following equations [19]:

$$C_{l,k} = \frac{\pi}{2} \sin(\alpha_k (1 + v + 2\sqrt{v})) \quad (3.15a)$$

$$C_{m,k} = \frac{\pi}{2} \sin(\alpha_k (1 + v + 2\sqrt{v})) \left(\frac{5+5v-6\sqrt{v}}{16} \right) \quad (3.15b)$$

$$\|C_{d,k}\| = \frac{0.89}{\sqrt{Re}} + \frac{1}{\pi e A_R} \tilde{C}_{1,k}^2 \quad (3.15c)$$

Where Re is the cord-wise Reynolds number, A_R is the aspect ratio, e is the Oswald efficiency factor, and where:

$$\tilde{C}_{1,k} = \frac{\|\vec{F}_{1,k}(\mathbf{q}, \dot{\mathbf{q}})\|_2}{0.5} \rho_{air} \left(\left(\frac{\partial \vec{p}_{cp,k}}{\partial \mathbf{q}} \dot{\mathbf{q}} \right)^{t,n} \right)^T \left(\frac{\partial \vec{p}_{cp,k}}{\partial \mathbf{q}} \dot{\mathbf{q}} \right)^{t,n} c_k \quad (3.15d)$$

Once these constants have been determined, the elemental lift, $F_{l,k}$ and quarter chord moment, $M_{m,k}$, can be determined with the help of the following equations [19]:

$$\|\vec{F}_{l,k}(\mathbf{q}, \dot{\mathbf{q}})\|_2 = 0.5\rho_{air} \left(\left(\frac{\partial \vec{p}_{cp,k}}{\partial \mathbf{q}} \dot{\mathbf{q}} \right)^{t,n} \right)^T \left(\frac{\partial \vec{p}_{cp,k}}{\partial \mathbf{q}} \dot{\mathbf{q}} \right)^{t,n} c_k C_{1,k} + \frac{\pi}{4} \rho_{air} c_k^2 (\ddot{\zeta} + V_\infty \dot{\alpha}_k - (x_a - 0.25) c_k \ddot{\alpha}_k) \quad (3.16)$$

$$\|\vec{M}_{m,k}(\mathbf{q}, \dot{\mathbf{q}})\|_2 = 0.5\rho_{air} \left(\left(\frac{\partial \vec{p}_{cp,k}}{\partial \mathbf{q}} \dot{\mathbf{q}} \right)^{t,n} \right)^T \left(\frac{\partial \vec{p}_{cp,k}}{\partial \mathbf{q}} \dot{\mathbf{q}} \right)^{t,n} c_k^2 C_{m,k} + \frac{\pi}{4} \rho_{air} c_k^2 (V_\infty \dot{\zeta} + \frac{(x_a - 0.25) c_k \ddot{\zeta}}{2} + V_\infty^2 \alpha_k - c_k^2 \left(\frac{1}{32} + (x_a - 0.25)^2 \ddot{\alpha}_k \right)) \quad (3.17)$$

where c_k is the elemental chord length, ρ_{air} is the density of air and V_∞ is the stream velocity.

After employing the principle of virtual work, the elemental generalized forces and torques are given as:

$$\mathcal{Q}_{k,\vec{F}} = \left(\frac{\partial \vec{p}_{cp,k}}{\partial \mathbf{q}} \dot{\mathbf{q}} \right)^T \left(\vec{F}_{1,k}(\mathbf{q}, \dot{\mathbf{q}}) + \vec{F}_{d,k}(\mathbf{q}, \dot{\mathbf{q}}) \right) + \left(\frac{\partial \vec{\omega}_{cp,k}}{\partial \dot{\mathbf{q}}} \right)^T \vec{M}_{m,k}(\mathbf{q}, \dot{\mathbf{q}}) \quad (3.18)$$

Where $\omega_{cp,k}$ is the angular velocity of each element with respect to the inertial frame.

After integrating the elemental generalized forces along the wingspan, the total generalized aerodynamic force is determined which is as follows:

$$\mathcal{Q}_{\vec{F}} = \sum_{k=1}^{l_w} \left(\mathcal{Q}_{k,\vec{F}}(\mathbf{q}, \dot{\mathbf{q}}) \right) \quad (3.19)$$

where l_w is the number of elements along the wingspan.

Wing Kinematic Parametrization:

For the parametrization, time-varying holonomic constraints have been used to shape the system [19]. These holonomic constraints determine the orientation and position of the links of the open kinematic watts six-bar chain using servo actuators to drive the actuated portions of the system.

After partitioning the configuration variable vector, \mathbf{q} as $\mathbf{q} = (\mathbf{X}; \mathbf{q}_a)$, where \mathbf{q}_a is the actuated coordinates and \mathbf{X} are the unactuated coordinates which include Euler angles, body COM positions, and passive joint angles, the following equation has been obtained:

$$\begin{bmatrix} \mathcal{M}_1 & \mathcal{M}_2 \\ \mathcal{M}_3 & \mathcal{M}_4 \end{bmatrix} \begin{bmatrix} \ddot{\mathcal{X}} \\ \ddot{\mathbf{q}}_a \end{bmatrix} + \begin{bmatrix} \mathcal{C}_1 & \mathcal{C}_2 \\ \mathcal{C}_3 & \mathcal{C}_4 \end{bmatrix} \begin{bmatrix} \dot{\mathcal{X}} \\ \dot{\mathbf{q}}_a \end{bmatrix} + \begin{bmatrix} \mathcal{G}_1 \\ \mathcal{G}_2 \end{bmatrix} = \left(\frac{\partial \mathbf{q}_a}{\partial \mathbf{q}} \right)^T \lambda + \mathcal{Q}_{\vec{F}} \quad (3.20)$$

Thus we can see that the inertial, Coriolis, gravity, and aerodynamic terms interlock the actuated and un-actuated dynamics. To form the actuated dynamics, the actuators are used whose action is dependent on the parameterization of the holonomic constraints. Therefore, a constraint manifold is defined and a finite-state non-linear optimizer shape the constraints to achieve stability of the system. The servo actuators determine the position of the links with the help of constrained trajectories which are defined through an ordinary differential equation [19]:

$$\mathcal{N} = \mathbf{q}_a - r_d(t, \beta) \quad (3.21)$$

where r_d denotes the vector of the preferred path, t is the time and β is the vector representing the kinematic parameters of the wing.

To avoid the numeric discretization errors, the constraints in position and velocity have also been considered which leads to:

$$\ddot{\mathbf{q}}_a = \left(\frac{\partial \mathcal{N}}{\partial \mathbf{q}_a} \right)^{-1} \left(-\kappa_1 \dot{\mathcal{N}} - \kappa_2 \mathcal{N} - \frac{\partial^2 \mathcal{N}}{\partial t^2} - \frac{\partial}{\partial \mathbf{q}_a} \left(\frac{\partial \mathcal{N}}{\partial \mathbf{q}_a} \dot{\mathbf{q}}_a \right) \dot{\mathbf{q}}_a \right) \quad (3.22)$$

By solving the following system of ODE, the design of pre-defined trajectories for the vehicle dynamics is now workable.

$$\left\{ \begin{array}{l} \begin{bmatrix} \ddot{\mathcal{X}} \\ \ddot{\mathbf{q}}_a \end{bmatrix} = \left(\begin{bmatrix} \mathcal{M}_1 & \mathcal{M}_2 \\ \mathcal{M}_3 & \mathcal{M}_4 \end{bmatrix} \right)^{-1} \left(-\begin{bmatrix} \mathcal{C}_1 & \mathcal{C}_2 \\ \mathcal{C}_3 & \mathcal{C}_4 \end{bmatrix} \begin{bmatrix} \dot{\mathcal{X}} \\ \dot{\mathbf{q}}_a \end{bmatrix} - \begin{bmatrix} \mathcal{G}_1 \\ \mathcal{G}_2 \end{bmatrix} + \left(\frac{\partial \mathbf{q}_a}{\partial \mathbf{q}} \right)^T \lambda + \mathcal{Q}_{\vec{F}}(\mathbf{q}, \dot{\mathbf{q}}) \right) \\ \ddot{\mathbf{q}}_a = \left(\frac{\partial \mathcal{N}}{\partial \mathbf{q}_a} \right)^{-1} \left(-\kappa_1 \dot{\mathcal{N}} - \kappa_2 \mathcal{N} - \frac{\partial^2 \mathcal{N}}{\partial t^2} - \frac{\partial}{\partial \mathbf{q}_a} \left(\frac{\partial \mathcal{N}}{\partial \mathbf{q}_a} \dot{\mathbf{q}}_a \right) \dot{\mathbf{q}}_a \right) \end{array} \right\} \quad (3.23)$$

A shooting method [19] is then applied which converts the system of ODE given above into a two-point boundary value problem given by:

$$\begin{bmatrix} \dot{\mathbf{q}} \\ \ddot{\mathbf{q}} \end{bmatrix} = \mathbf{H}(t, \mathbf{q}, \dot{\mathbf{q}}, \beta) \quad (3.24)$$

where \mathbf{H} presents the system of equations and t (or T_p) is the period.

The initial-state time dependence of the vectors of generalized coordinates is given by:

$$\mathbf{q} = \mathbf{q}(\mathcal{T}_p, \mathbf{q}_0, \dot{\mathbf{q}}_0) \quad \dot{\mathbf{q}} = \dot{\mathbf{q}}(\mathcal{T}_p, \mathbf{q}_0, \dot{\mathbf{q}}_0) \quad (3.25a \text{ and } 3.25b)$$

After applying the Taylor approximation and taking in to account the corrections, the following linear system of equations has been determined:

$$\begin{bmatrix} \delta \mathbf{q}_0 \\ \delta \dot{\mathbf{q}}_0 \end{bmatrix} = \begin{bmatrix} \frac{\partial \mathbf{q}(\mathcal{T}_p, \mathbf{q}_0, \dot{\mathbf{q}}_0)}{\partial \mathbf{q}_0} & \frac{\partial \mathbf{q}(\mathcal{T}_p, \mathbf{q}_0, \dot{\mathbf{q}}_0)}{\partial \dot{\mathbf{q}}_0} \\ \frac{\partial \dot{\mathbf{q}}(\mathcal{T}_p, \mathbf{q}_0, \dot{\mathbf{q}}_0)}{\partial \mathbf{q}_0} & \frac{\partial \dot{\mathbf{q}}(\mathcal{T}_p, \mathbf{q}_0, \dot{\mathbf{q}}_0)}{\partial \dot{\mathbf{q}}_0} \end{bmatrix}^{-1} \begin{bmatrix} \mathbf{q}_0 - \mathbf{q}(\mathcal{T}_p, \mathbf{q}_0, \dot{\mathbf{q}}_0) \\ \dot{\mathbf{q}}_0 - \dot{\mathbf{q}}(\mathcal{T}_p, \mathbf{q}_0, \dot{\mathbf{q}}_0) \end{bmatrix} \quad (3.26)$$

The solutions to these systems of equations can be determined through MATLAB solutions.

This concludes the mathematical modelling of the robot's kinematic parameters. Upon successful execution of the modelling, the robot will be able to optimize its kinematic parameters and will achieve maximum flight efficiency.

3.3 Geometric Modeling and Design

Based on the parameters calculated in Section 3.1, a 3D model was made for the design on SolidWorks, shown in Figures 3-5.

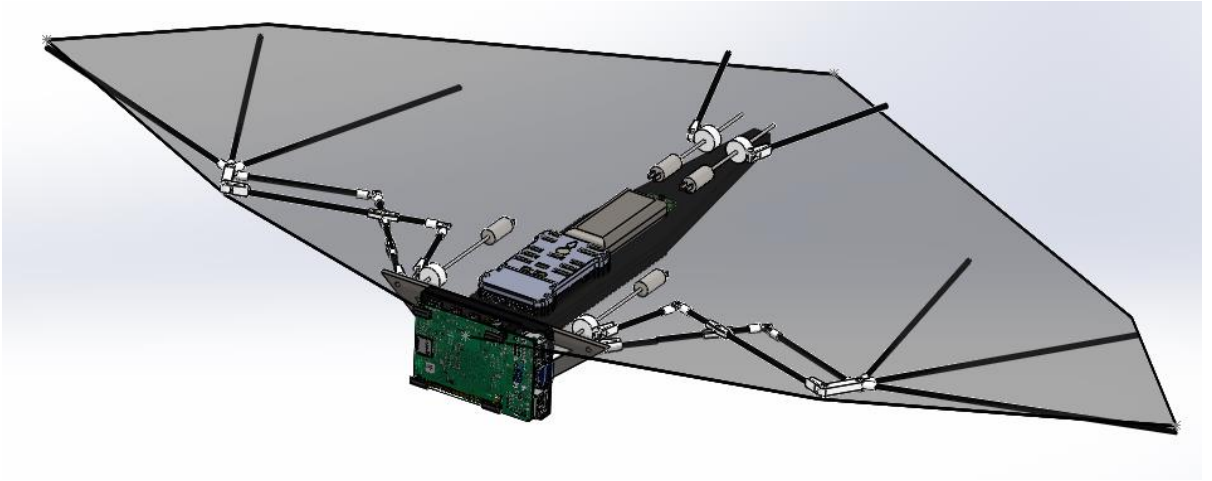


Figure 3- 5: CAD Model of Robot

As shown in Figure 3-6, the design can be divided into 3 basic components: forelimb wings (red), hindlimbs (blue), and body (yellow). The entire structure is covered by the membrane as the lifting surface whereas the electronics and control systems are mounted on the body.

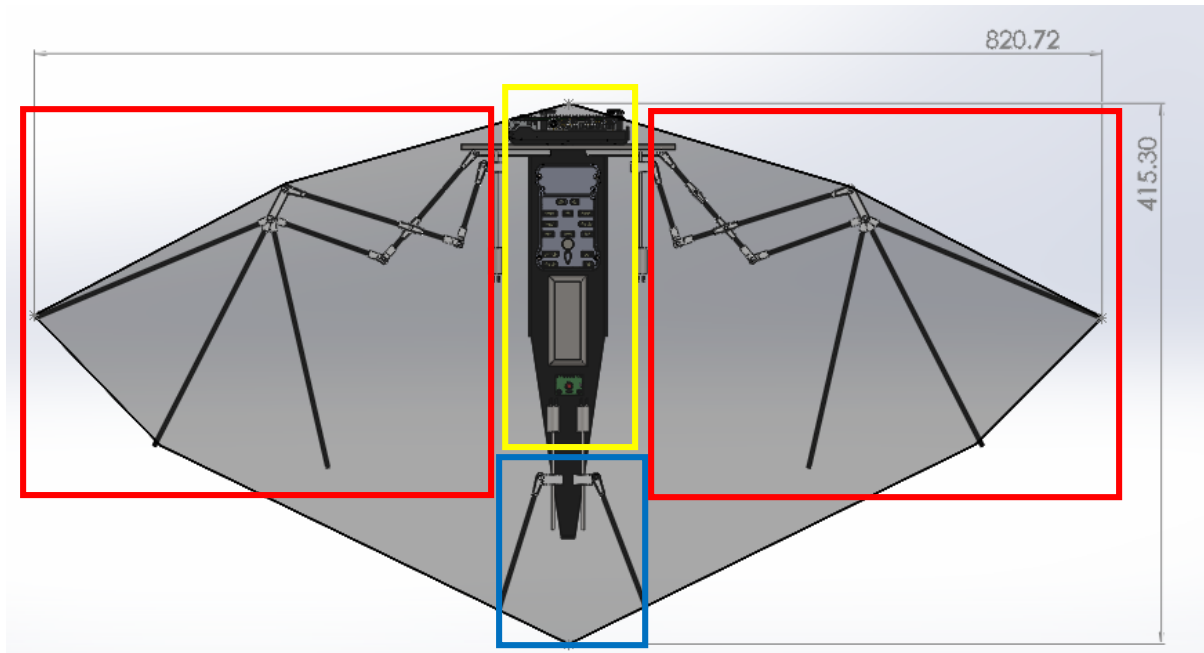


Figure 3- 6: Model Divisions - forelimbs (red), hindlimbs (blue), body (yellow). All dimensions in mm

A detailed model of the forelimb is shown in Figure 3-7. It consists of 3 basic divisions, namely fingers, forearm, and upper arm, analogous to a human arm, connected by the wrist (red), elbow (blue), and shoulder joints (yellow).

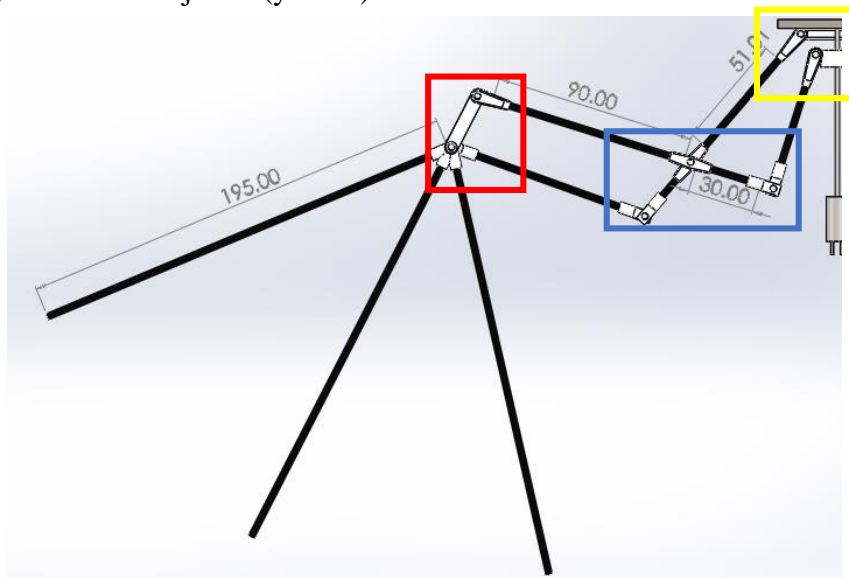


Figure 3- 7: Forelimb Model - wrist (red), elbow (blue), shoulder (yellow). All dimensions in mm

A

detailed production drawing for the forelimb assembly with dimensions can be found in Appendix A as well as detailed models of the different joints. All dimensions are in mm.

3.4 Analysis

The first step in the analysis of the micro-UAV was to determine the geometric and aerodynamic parameters. The values of different parameters along with their scaling factors have been shown in Table 3-2 and Table 3-3. As the mass was taken as 500g, the minimum and maximum wingspan came out to be 0.746m and 0.776m respectively. These two were averaged out to obtain the mean wingspan, 0.760m.

A forelimb mechanism based on the mean wingspan of 0.76m was designed in MSC Adams. The link lengths of the watts six-bar chain have been enlarged by a factor of 2.5, as compared to the lengths found in the literature. The comparison between the link lengths of the designed model and the Bat Bot of Caltech is shown in Table 3-4.

Table 3- 4: Caltech and GIK Model Comparison

Link Type	Caltech Model [3]	GIK Institute Model
Humerus (Arm)	0.035m	0.11m
Radius (Forearm)	0.045m	0.12m
Digits (Fingers)	0.14m	0.195m
Femur (Leg)	0.1m	0.25m

To provide the linear motion to the slider (lead screw drive) for the actuation of the watts six-bar chain, a sinusoidal input motion was given to the slider; velocity, V_s , of the slider, is defined as $V_s = 10 \sin(\omega t) = 10 \sin(62.8t)$. Here, ω is equal to 62.8 rad/sec which is equivalent to a frequency of 10 Hz. The same frequency has been used for the input motion of the flapping mechanism, to achieve the synchronicity between the flapping and folding/unfolding mechanism. Figure 3-12 displays the front view whereas Figure 3-13 displays the isometric view of the forelimb mechanism.

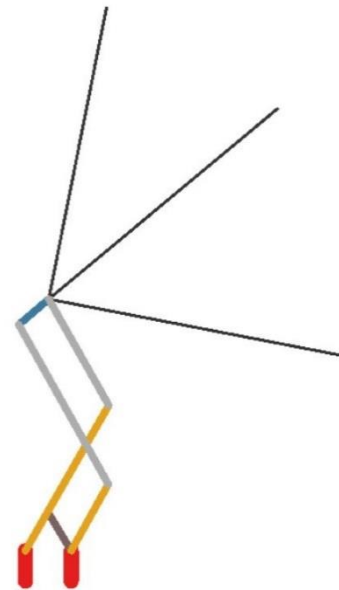


Figure 3- 8: Forelimb Mechanism (front view)

As the links would be treated as hollow cylinders, the diameter for the hollow tubes has been taken as 3mm, and the formula for the calculation of moment of inertia for each link has been given in Eq. 3.2. The model shown in Figure 3-12 is designed for kinematic analysis only. For the dynamic analysis, the links will be converted into hollow tubes, and then the mass moment of inertia and forces will be calculated from the software.

3.4.1 Kinematic Analysis of Digits

A detailed kinematic analysis for the fingers of the robot, and the slider, which is used for actuation, has been performed in this section.

Using Eq. 3.3a and 3.3b, the software calculates the angular position of the links. After finding the angular positions, Eq. 3.4a, 3.4b, and 3.4c are used to find the velocities at any given point of the links. Finally, Eq. 3.6a, 3.6b, and 3.6c are used for the acceleration analysis.

Position Analysis:

Figure 3-14 shows that the center of mass of the fingers trace an oscillatory path both in the x and y directions. The maximum displacement in the x-direction, i.e., 26.25 mm, is less than that in the y-direction, i.e., 37.5mm. The motion is oscillatory because as the slider actuates the forelimb mechanism, it moves back and forth, thus causing the fingers of the watt's six bar chain to behave as rockers, and hence they oscillate about their mean positions.

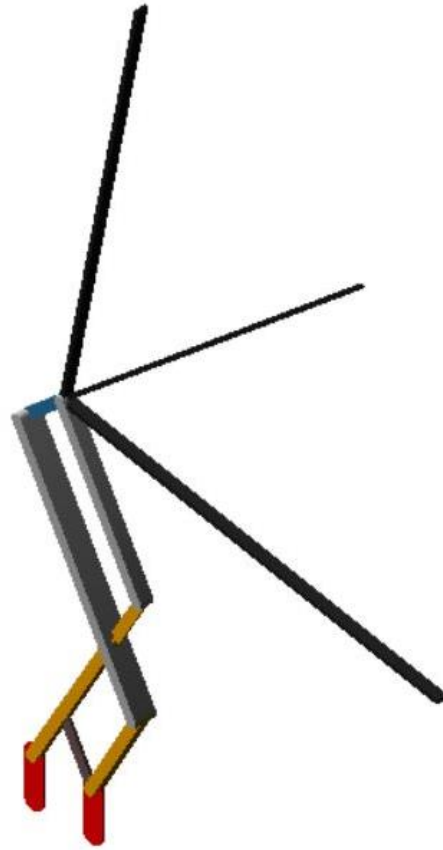


Figure 3- 9: Forelimb Mechanism (isometric view)

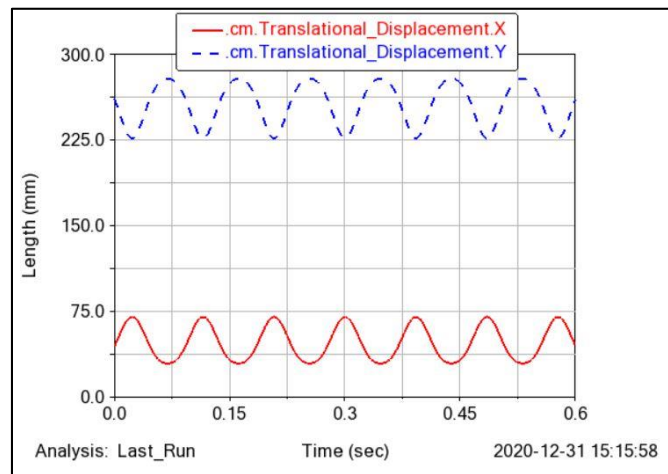


Figure 3- 10: Translational Displacement of CoM of Finger

Velocity Analysis:

Figure 3-15 shows that the velocity at the center of mass of the fingers is a cosine function both in x and y direction with the maximum amplitude greater in the y-direction. The graphs in Figure 3-15 have been obtained by differentiating the curves obtained in Figure 3-14 with respect to time, hence upon taking the derivative of sin function, we obtained the velocity graphs representing cosine function. At time, $t = 0$ seconds, the velocity in the y-direction is -1750 mm/sec while that in the x –direction is 1500 mm/sec . This shows that the fingers are moving downwards towards right.

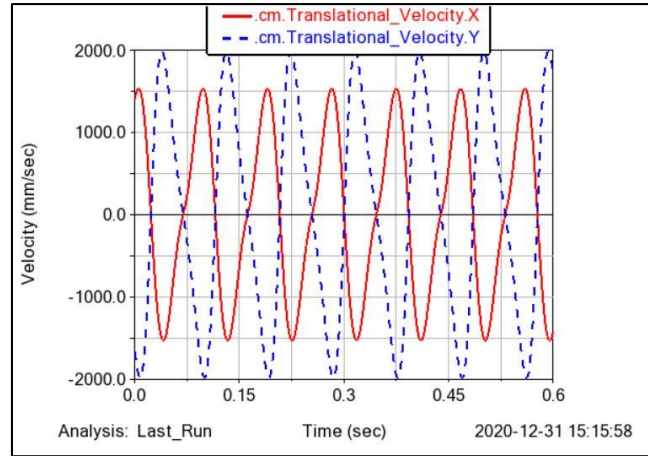


Figure 3- 11: Translational Velocity of CoM of Finger

Acceleration Analysis:

Figure 3-16 shows that the acceleration at the center of mass of the fingers shows a periodic trend both in x and y direction with the maximum amplitude greater in the y-direction. This periodic trend has been obtained by differentiating the velocity graphs, shown in Figure 3-15, with respect to time. At time $t = 0$ seconds, the acceleration in the y-direction is -60 m/sec while that in the x-direction is 50 m/sec . Therefore, it can be concluded that the net external force in the y-direction is greater, as compare to that in x-direction.

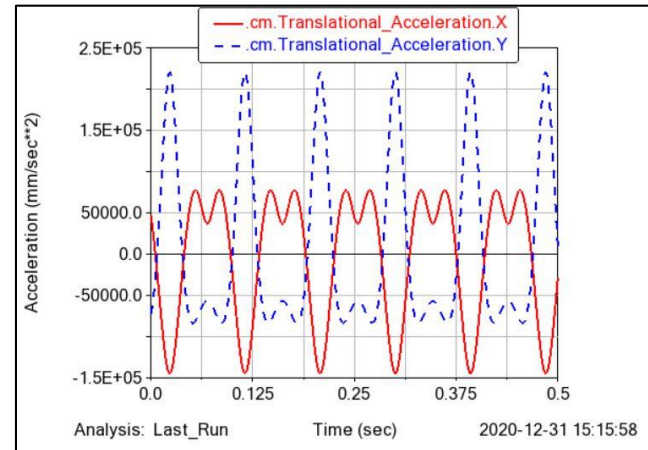


Figure 3- 12: Translational Acceleration of CoM of Finger

3.4.2 Kinematic Analysis of Slider

The lead screw drive used to actuate the forelimb mechanism has been substituted by a slider which moves in a horizontal path along the x-axis. Using Eq. 3.3a and 3.3b, the software calculates the angular position of the links. After finding the angular positions, Eq. 3.4a, 3.4b, and 3.4c are used to find the velocities at any given point of the links. Finally, Eq. 3.6a, 3.6b, and 3.6c are used for the acceleration analysis.

Position Analysis:

The figure shows the linear displacement of the slider with respect to time. It can be seen that the displacement varies sinusoidally, because of the sinusoidal input function. The maximum displacement of the slider from the mean position is 50 mm and the time taken by the slider to make one complete oscillation is around 0.1 seconds. Time period of 0.1 seconds means a frequency of 10 Hz, therefore, the graph verifies the frequency requirements of the forelimb mechanism, which were obtained theoretically.

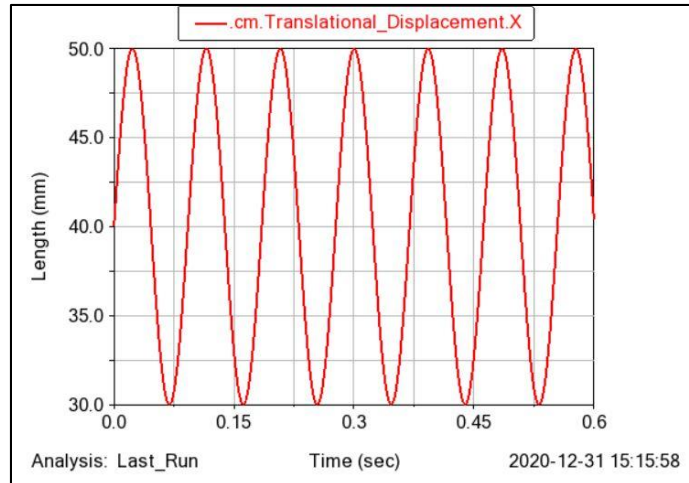


Figure 3- 13: Translational Displacement of Slider

Velocity Analysis:

Figure 3-18 shows the velocity variation of the slider in the x -direction. Again, the variation is oscillatory, but this time the velocity function shows a cosine behavior, as it has been by differentiating the displacement function (sinusoidal), as shown in Figure 3-17. The graph shows that at time $t = 0$ seconds, the velocity of the slider is maximum, i.e., 650 mm/sec , which means that the slider is at its mean position. The velocity reaches to 0 m/s at time $t = 0.025$ seconds, which indicates that the slider has reached to its maximum position. Now, the slider moves in the opposite direction, again reaches the mean position and finally reaches the extreme position, at $t = 0.1$ seconds.

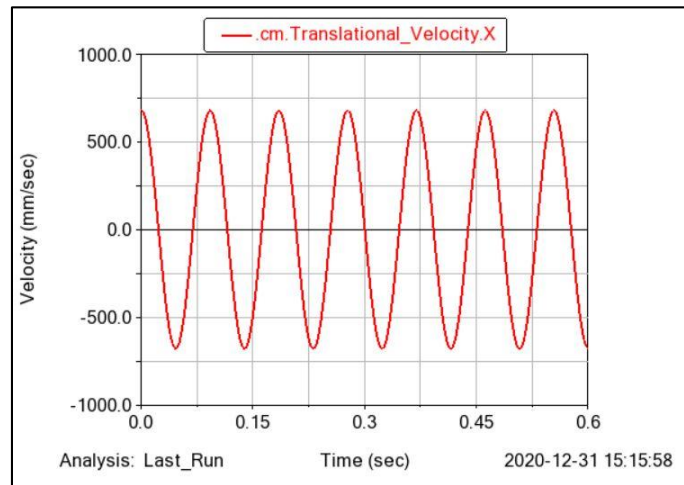


Figure 3- 14: Translational Velocity of Slider

Acceleration Analysis:

Figure 3-19 shows the acceleration variation of the slider in the x –direction. Again, the variation is oscillatory (sinusoidal). The acceleration curve has been obtained by differentiating the velocity graphs of Figure 3-18 with respect to time. At time $t = 0$ seconds, the value of acceleration

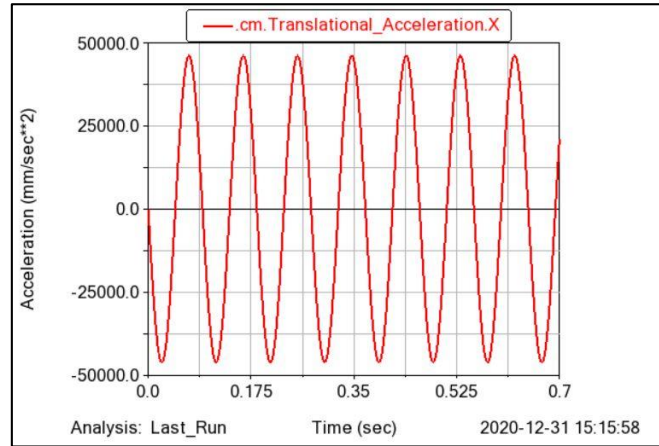


Figure 3- 15: Translational Acceleration of Slider

is 0 m/s^2 , which means that the slider is at the mean position and its velocity is maximum. The acceleration of the slider reaches to a maximum of 43.75 m/s^2 at 0.025 seconds, which shows the point of zero velocity.

This concludes the kinematic analysis of the forelimb mechanism. The values of acceleration, obtained from the analysis, have to be utilized to find the torques, moments, and forces.

3.4.3 Kinematic Analysis of Flapping Mechanism

For the flapping mechanism, shown in Figure 3-20, two spur gears have meshed together and the connecting rods are eccentrically attached with the gears. The connecting rods, from the other end, are attached with the adapters, which are linked with the shoulder bar and humeral link. Once the gear rotates, the connecting rod causes the adapters to rotate, thus ensuring flapping.

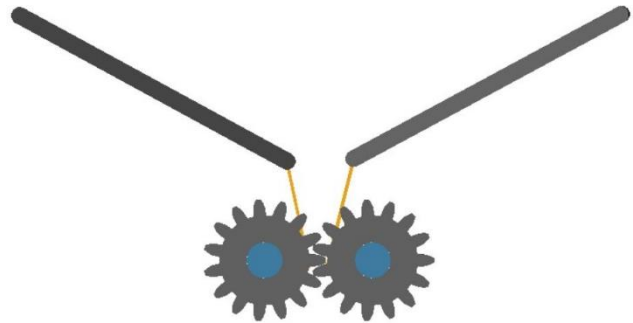


Figure 3- 16: Flapping Mechanism (front view)

Again, using Eq. 3.3a and 3.3b, the software calculates the angular position of the links. After finding the angular positions, Eq. 3.4a, 3.4b, and 3.4c are used to find the velocities at any given point of the links. Finally, Eq. 3.6a, 3.6b, and 3.6c are used for the acceleration analysis. The gears are being rotated at an angular velocity, ω , of 62.83 rad/sec . This ω is equivalent to 10 Hz , and as discussed previously, the motions of flapping and folding/unfolding mechanisms are synchronous.

Figure 3-21 shows the isometric view of the flapping mechanism. It can be seen that the gears have meshed together and hence, the flapping motion is synchronous. Moreover, according to the literature, to attain the preferred lift, the ratio of downstroke time to total wingbeat period must be greater than 0.6. Hence, here, we are interested in finding only the rotational velocity of the connecting rod.

The graph in Figure 3-22 shows the rotational velocity of the connecting rod with respect to time. It can be seen that the wing beat period is 0.1 seconds which is equivalent to 10 Hz. At time $t = 0$ seconds, the angular velocity of the connecting rod is maximum, i.e., about 22.7 rad/sec . When the rod reaches to its maximum point, i.e., close to the adapter, its angular velocity reduces to 0 rad/sec . Now, it undergoes the downstroke motion and reaches a maximum angular velocity of

19.20 rad/sec before coming to rest at the other extreme position (at the bottom). As observed from the graph, the downstroke period is approximately 0.06 sec . The ratio of downstroke period to the total time period is 0.6, which means that the condition for minimum ratio required for achieving the desired lift has been satisfied.

3.4.4 Membrane Shape Analysis

Keeping the same aspect ratio, AR, as for the Caltech Bat Bot, the wing area for the micro-UAV has been calculated using the formula:

$$AR = \frac{b^2}{s} \quad (3.27)$$

Table 3-5 shows the comparison between the wingspan, wing area, and AR of the two models.

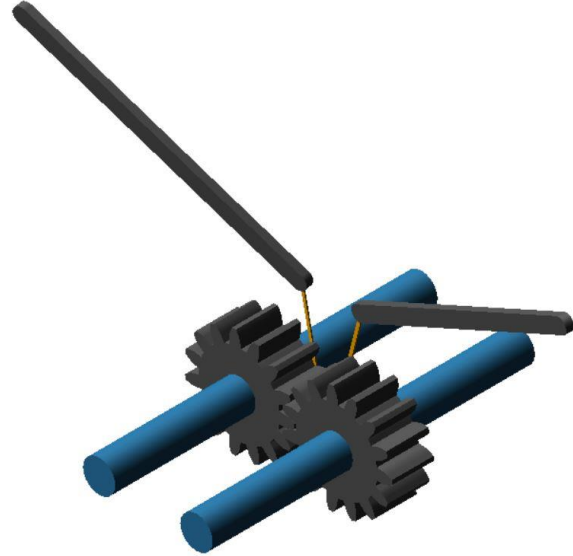


Figure 3- 18: Flapping Mechanism (isometric view)

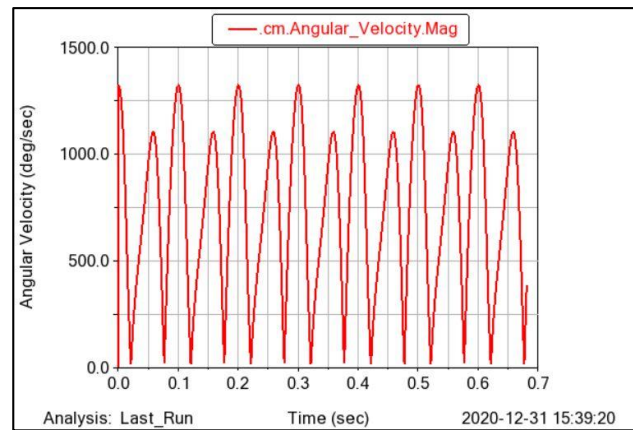


Figure 3- 17: Angular Velocity of Connecting Rod

Table 3- 5: Caltech and GIK Model Comparison

Parameters	Caltech Model [3]	GIK Institute Model
Wingspan (b)	0.469 m	0.776 m
Wing area (S)	0.0694 m ²	0.2 m ²
Aspect ratio (AR)	3.17	3.17

The shape of the membrane has been assumed as a Kite, which has been further divided in to two triangles (upper and lower), with both sharing the common base equal to the wingspan of the robot.

Area of Upper Triangle:

The wing span has been approximated as 1m, in order to ensure that the extra material is available for joining at the corners.

$$A_U = 0.5 * b * h_U = 0.5 * 1 * 0.1 = 0.05 \text{ m}^2 \quad (3.28)$$

The height, h_U , has been taken from the model designed at MSC Adams (the length between the shoulder bar and the finger tip).

Area of the Lower Triangle:

$$A_L = 0.2 - A_U = 0.15 \text{ m}^2 \quad (3.29)$$

$$h_L = \frac{A_L}{0.5 * b} = 0.4 \text{ m} \quad (3.30)$$

The height of the lower triangle, h_L , has been approximated as 0.5m.

Therefore, a circular silicone membrane of diameter, $d = 1\text{m}$ is manufactured with the help of molds, and a kite of base 1m and a total height of 0.6 m, has been cut out from the circle.

Figure 3-23 shows the exact dimensions of the kite, measured in mm. It can be seen that the base is 0.82m which is approximately same as the theoretical wing span of the robot (0.776m).

Moreover, the total height is 0.42m, and is the same as calculated i.e., $h_L = 0.4\text{m}$.

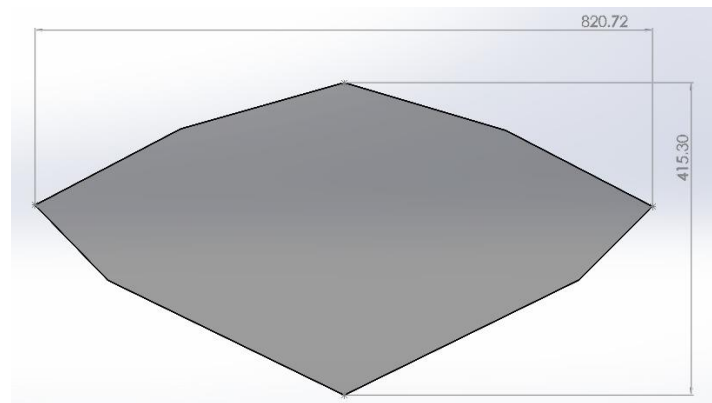


Figure 3- 19: Membrane Shape

Table 3-6 shows the comparison between the approximated and exact dimensions of the kite shaped membrane.

Table 3- 6: Approximate and Exact Dimensions of Membrane

Dimensions	Exact	Approximate
Wing Span	0.821 m	1 m
Total Kite Height	0.415 m	0.6 m

3.4.5 Analysis of Environmental and Social Impact

While, designing the structure of the micro-UAV, several aspects were taken in to consideration, that makes the design robust and efficient. The impact of the machine on environment and society has been briefly discussed below.

Environmental Impact:

As the structure of the robot is made from carbon fiber, the weight is significantly low as compare to other machines, like drones. The light weight allows the machine to achieve maximum lift with minimal energy input, thus conserving energy and reducing the burden on environment. Moreover, the machine incorporates piezo electric transducers underneath its membrane, which continuously harvest energy during the flight. This harvested energy, can be utilized to operate small sensors and LEDs, thus reducing the burden on the batteries. Lastly, the prime mover in the micro-UAV is a brushless DC (BLDC) motor, which means there is no emission of harmful gases, and thus no contribution to greenhouse effect, as is the case with a combustion engine.

Social Impact:

The robot consists of folding and unfolding mechanism which allows it to enter narrow and harmful regions, especially for surveillance during disaster management. This will help the concerned authorities and NGOs to make use of machines instead of humans to analyze the dangerous zones, and hence reduce the risk to human life. The flapping mechanism which operates at a frequency of 10Hz, allows the robot to achieve maximum flight efficiency, and thus higher lift. Higher flapping frequency enables the robot to cover a larger flight range, thus giving humans the leverage to analyze the disaster affected area from a distant place. This will not only save their time and effort, but will also allow the authorities to safely communicate with the people present at the site.

3.5 Summary

For the designing of a bat inspired micro-UAV, the alternatives for forelimb flapping, forelimb mediolateral, and hindlimb dorsoventral mechanisms, found from the literature, have been organized in the form of a morphological chart. After the selection of alternatives, each of them has been designed on MSC Adams and a detailed kinematic analysis has been performed based on the governing equations. Moreover, the Langrangian approach has been adopted for the optimization of aerodynamic parameters of the micro-UAV. Based on the calculated values of geometric and aerodynamic parameters, a CAD model for the robot has been constructed on SolidWorks. Finally, the environmental and social impacts of the robot have been analyzed, and it can be concluded that the design is feasible from both the aspects.

Chapter 4

PHYSICAL MODEL DEVELOPMENT AND TESTING

4.1 Development Process

In this section, the fabrication processes opted for each component have been described.

4.1.1 Membrane

For the fabrication of the membrane, it was required that the chosen material be flexible but strong and averse to tearing. Our chosen material was the Smooth-On Dragon Skin Series Silicon in 10 Medium. The material properties [15] for it are given in Table 4-1 below:

Table 4- 1: Dragon Skin 10 Medium Properties

Property	Value
Mixed Viscosity	23,000 mPa s
Specific Gravity	1.07
Specific Volume	0.000932 m ³ /kg
Pot Life	20 min
Cure Time	5 hours
Tensile Strength	3.28 MPa
% Elongation at Break	1000%
Useful Temperature Range	-53°C to +232°C

The product comes in two packages, A and B, namely the silicon mixture and the hardener. The two liquids are to be mixed in a 1A:1B mass ratio. Since the mixture is very viscous, it proved to be quite difficult to spread, hence a rig was constructed for it. It consists of two weighted 1x1 meter glass sheets stacked on top of one another, with a separation of 1mm achieved by lining the outer edges with 1mm double sided tape.



Figure 4- 1: Membrane Manufacturing

Firstly, both glass sheets were lubricated using Vaseline gel to ensure the silicon can be easily removed after curing. Next, the A and B mixture was measured out using a mass balance to ensure equal mass and mixed together. The mixture was poured on to the bottom sheet in the center and the second sheet placed on top immediately to spread out the mixture evenly, shown in Figure 4-1. Once set, the mixture was left overnight to cure completely at room temperature. Once cured, the



Figure 4- 2: Manufactured Membrane

sheets were separated and the membrane detached carefully to ensure no tears were made. The final circular membrane has a diameter of 1m and will be cut to shape according to the shape of the skeleton described previously i.e. a kite.

4.1.2 Skeleton

The skeleton for the structure was constructed using hollow carbon fiber rods of 3mm diameter and wall thickness 0.5mm. Hollow rods were chosen due to greater strength in shear and carbon fiber itself is very light-weight and flexible, allowing the wings to flex similar to a biological bat.



Figure 4- 3: Hollow Carbon Fiber Rods

4.1.3 Joints

The wing structure of the bat consists of many joints, similar to a human limb. Since each limb was extremely small with very intricate details, 3D printing was chosen to manufacture them. The material used for printing was PLA. Each joint has been simplified down to 1 DOF pin joint, to be connected using 3mm rivets.



Figure 4- 4: Manufactured Joints (left to right) - wrist, auxiliary wrist, auxiliary wrist/shoulder, elbow

However, after manufacturing and due to low tolerances in the printing process, the 3D printed joints were deemed unfit for operation. As such, the second alternative was to manufacture the joints from aluminium alloy. The manufactured joints were much more durable and afforded greater resistance to fracture.

4.1.4 Body

The body is the main backbone of the structure upon which each of the subsystems would be mounted. It was constructed out of Jumbolon, a type of lightweight, stiff depron foam. The outline for the body was cut out using hot-wire cutting. The internal slots were cut using the wood router after constructing the model in SolidWorks.



Figure 4- 5: Wood Router for cutting body slots

4.1.5 Assembly

After the manufacturing of each of the individual components, the entire structure was brought together in a modular fashion to make the final assembly.

Wing

The wing joints and links were assembled using 3mm rivets for the 1DOF joints and superglue for the fixed joints.

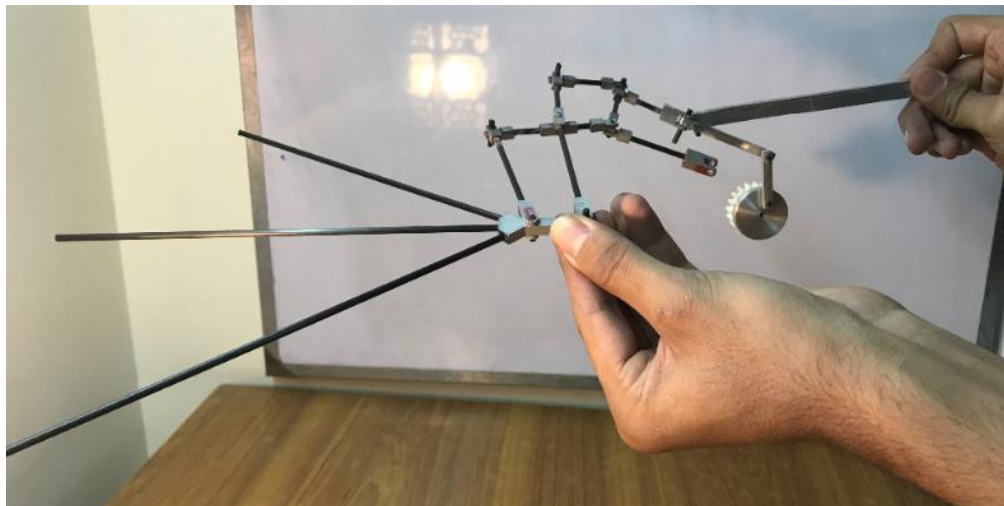


Figure 4- 6: Wing Assembly

Flapping Mechanism

The flapping mechanism was constructed using a trapezoidal frame that would support the two meshed gears run by a single BLDC motor. A combination of mild steel links were used to create a crank-slider mechanism that would execute the flapping motion. This motion is translated to the wings using a shoulder bar attached to the end of the connecting rod.



Figure 4- 7: Flapping Assembly



Figure 4- 8: Gear and Motor Coupling

Assembly

The wing and flapping mechanisms were coupled to each other at the shoulder joint as well as the translating spindle joint for flexion. The spindle is then attached to the body via two cross links that span the width of the body and serve as the anchor point for the spindle as well. The gears are then inserted into the slot at the top of the body, to hold the mechanism in place. The other electronics are also attached at the top of the body frame. The membrane was then cut

out in the required shape and mounted on top of the entire frame, secured using hot glue. The piezoelectric sensor was also attached between the finger links at the furthest point from the body for maximum vibrational output.



Figure 4- 9: Flapping Mechanism Body Slot



Figure 4- 10: Skeleton Assembly



Figure 4- 11: Membrane and Piezoelectric Sensor

4.2 Integration and Instrumentation

The major electronics components and sensors to be used in the design are summarized as follows:

BLDC Motor:

Table summarises the specifications of the motor used. It was chosen due to its light weight and high RPM for running the flapping mechanism at the desired frequency.

Property	Value
Motor Size	35 x 30 mm
Shaft Size	5 x 47.5 mm
Weight	74 g
KV	1700 Kv
Maximum Power	460 W

Table 4- 2: Motor Properties

Electronic Speed Controller:

The design incorporates an ESC used to control the speed of the BLDC motor, which is essential for its working. The chosen ESC was based on motor compatibility, which was a 40A ESC.

IMU Sensor:

MPU9250 was chosen as the preferred IMU sensor, which consists of a 9 DOF tracking device with 3-axis accelerometer, gyroscope and magnetometer. This component is essential for the navigation and stability control of the robot during operation.

Piezoelectric Transducer:

The properties of the PZTs used for energy harvesting are summarized in Table 4-3.

Property	Value
Plate Size	20 mm
Thickness	0.42 mm
Resonance Frequency	6.3 kHz
Capacitance	10 nF

Dielectric Constant	1510
Resonant Impedance	<300 ohm
Maximum Input Voltage	30V

Table 4- 3: PZT Properties

4.3 Testing/Experimental Procedures

The completed model underwent several tests to ensure it met the required deliverables.

Flapping and Flexion

The experimental model was run using the BLDC motor attached to ensure it met the 10Hz operating frequency, verified using video recordings. The flexion of the forelimb was actuated from home to final positions to ensure smooth operation.

Energy Harvesting:

The PZTs were connected to an oscilloscope to measure the output voltage generated from the vibrations. The waveforms generated, shown in Chapter 5, were used to analyze the feasibility of using PZTs as a renewable energy source for the robot's operation.

Structural Testing:

The model underwent wing tip and load tests by balancing the weight at the wing tips. This was done to ensure the model is able to sustain at least its own weight during flight without any of the joints breaking under continuous stress.

4.4 Summary

Proceeding towards the embodiment design phase, the aerodynamic and geometric parameters of the UAV were calculated and the inverse and forward kinematic analysis of the linkages was performed on MSC Adams in order to determine the required motor for actuation. In addition to the inverse kinematic analysis, the trajectory planning of the robot was also performed using a systematic approach. First the Denavit Hartenberg (DH) table was constructed, through which the transformation matrices of the manipulator were worked out. Using the transformation matrices, the reachable and dexterous workspaces of the robot were determined. Moreover, a complete 3-D model of the robot was designed on SolidWorks through which the detailed drawings were used for manufacturing and assembling of the parts. Making use of the detailed design, the fabrication process was started, in which first the silicon membrane was manufactured using the glass sheets pressing method. The links for the Watts

six bar chain were cut from carbon fiber rods, while the joints of the linkage were wire cut using aluminum. For the flapping motion, the links were made from traditional machining of aluminum and were coupled with the forelimbs to perform flapping and folding simultaneously. Finally, the spindle drives were connected to the forelimbs via a bearing coupled with an aluminum disc, and the motors were connected for actuating the mechanism. After completing the assembly, the membrane was attached on the wing structure and piezo-electric transducers were placed beneath the membrane for harvesting energy.

CHAPTER 5

RESULTS AND DISCUSSION

5.1 Results

One of the objectives of the project was to harvest energy by converting the mechanical stresses, generated during the flapping motion of the robot, in to electrical signals via piezo-electric transducers. The energy generated should be sufficient enough to power small sensors such as proximity, temperature and infrared sensors, that would accompany the robot in its flight. Piezo-electric transducers were attached on the wing membrane at each end. To obtain the maximum output, the transducers were placed between the fingers, as shown in Figure 5-1, where maximum stresses are generated during the downstroke motion.

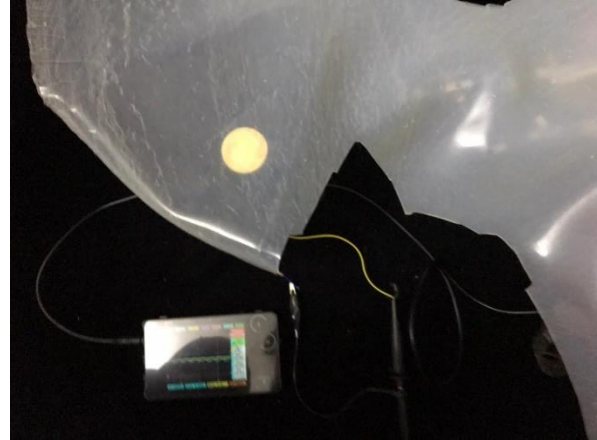


Figure 5- 1: Piezoelectric Transducer placement

To analyze the voltage signals generated from the flapping motion, an oscilloscope was connected to the piezo electric transducer as shown in Fig. In order to get the maximum output, the flapping frequency was optimized and kept at 2 Hz.

Once the robot starts flapping, a sinusoidal waveform is generated on the oscilloscope

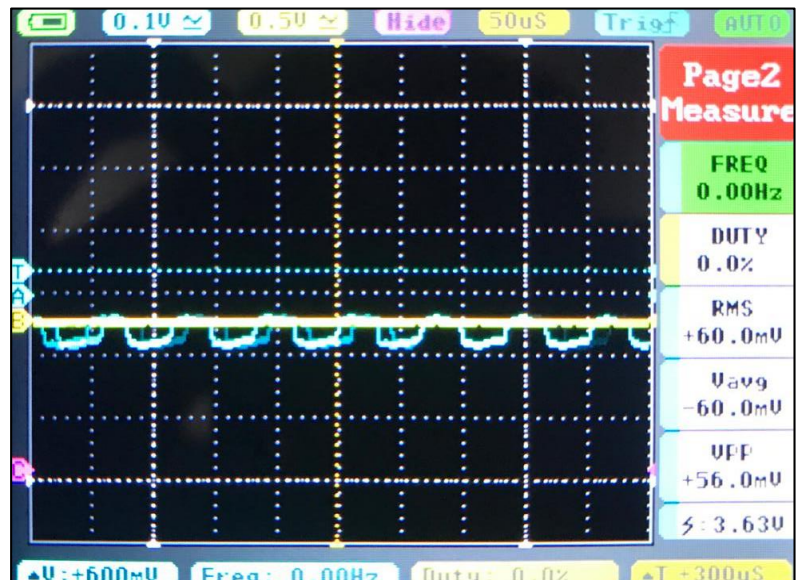


Figure 5- 2: Oscilloscope Waveform

with a root mean square (rms) value of 60.0 mV, as shown in Figure 5-2. The signal is

alternating because the flapping motion involves cyclic stresses, which are periodically changing during the upstroke and downstroke motion.

Table 5- 1: Waveform Parameters

Property	Value
RMS	60.0 mV
V_{avg}	-60.0 mV
V_{PP}	+56.0 mV
Duty cycle	0.0%

Table 5-1 shows the parameters of the sinusoidal waveform generated during flapping test. The rms value of the voltage obtained is not sufficient to power small sensors. Therefore, a signal amplification circuit has been designed on MATLAB to amplify the output to about 2 V which can be practically utilized.

Figure 5-3 shows the non-inverting amplification circuit designed on MATLAB Simscape to amplify the signal generated from piezo-electric transducer.

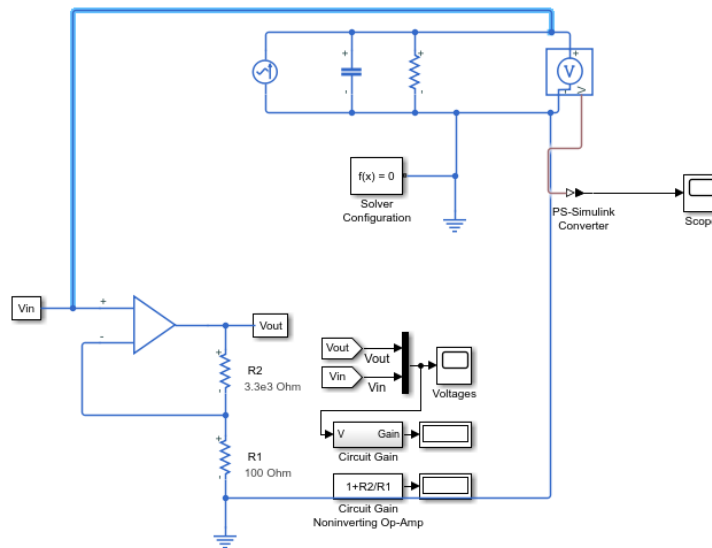


Figure 5- 3: Non-inverting Amplification Circuit

The circuit incorporates an operational amplifier connected with the transducer and two resistors with the ratio of 1:33 so as to increase the output voltage to up to 2V RMS, sufficient enough to power on-board electronics and sensors. The amplified signal obtained is shown below:

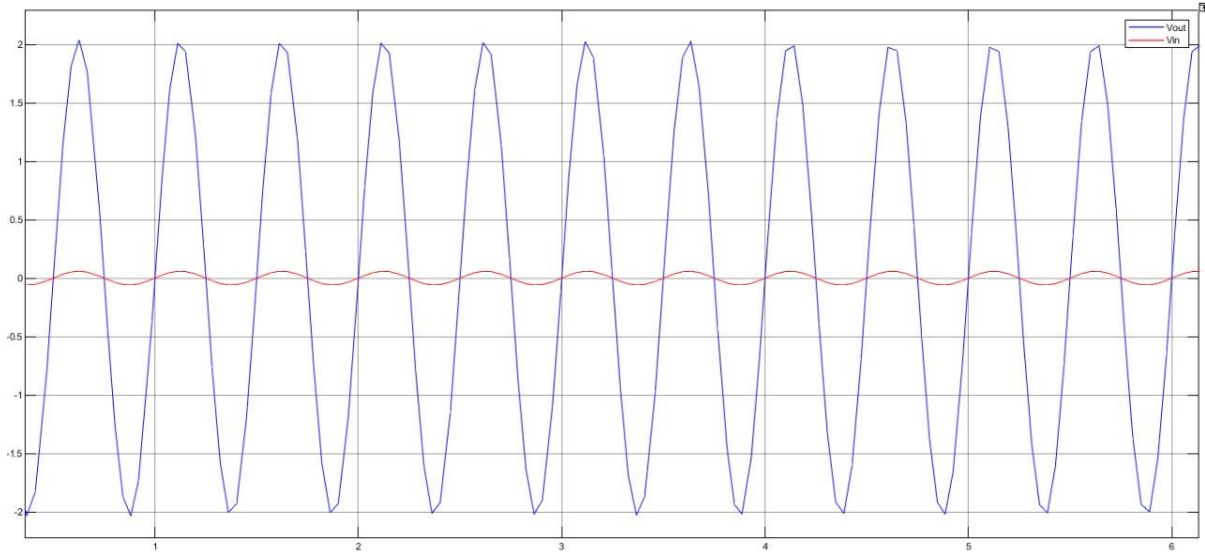


Figure 5- 4: Amplified Waveform

In Figure 5-4, the red waveform represents the original signal of amplitude 60mV, periodic and sinusoidal. The blue signal, on the same axis, represents the amplified signal of amplitude 2V and is in-phase with the original waveform, thereby verifying the use of a non-inverting amplifier.

5.2 Analysis and Discussion

5.2.1 Energy Harvesting

The signal obtained is alternating because the flapping motion involves cyclic stresses, which are periodically changing during the upstroke and downstroke motion. A similar sinusoidal waveform was achieved in a study conducted in University of North Texas when a similar piezo-electric transducer was used for harvesting energy using mechanical vibrations. The signal generated had an amplitude of 0.3V at a high frequency of 60 Hz without amplification. This shows that the results obtained at a low frequency of 2 Hz, having maximum amplitude of 60 mV are reliable.

Since the signal obtained is alternating in nature, a rectifier circuit can be utilized to achieve a direct signal which would then be used to power sensors and other electronic components. Table 5-2 below shows the results obtained at University of North Texas [19] with non-inverting amplification and rectification:

Table 5- 2: Amplification and Rectification Results [19]

Frequency / Hz	Voltage / V	Power / μ W
30	1.8	240
60	1.7	220
90	1.6	200

These results and the results obtained in this project show that it is possible for ornithopters to have a self-sustained flight by utilizing energy harvesters. Even though the signal produced is of low amplitude due to low operational frequency, it can be amplified using operational amplifiers to achieve desired voltage and power levels.

5.2.2 Trajectory Planning

One of the most important aspects in the flight of micro-UAVs is to determine the dexterous and reachable workspace of the manipulator. For this purpose, first of all a Denavit-Hartenberg (DH) table was constructed, as shown in Table 5-3 for the Watts six bar linkage used for mediolateral motions.

Table 5- 3: DH Table

i	$\alpha_{i-1}(rad)$	$a_{i-1}(mm)$	$d_i(mm)$	$\theta_i(rad)$
1	$\frac{\pi}{2}$	0.00	d_1	0
2	0	23.70	0	θ_2
3	0	42.10	0	θ_3
4	0	29.93	0	θ_4
5	0	29.38	0	θ_5
6	0	75.93	0	θ_6
7	0	25.80	0	θ_7
8	0	195.00	0	0

In order to define the lengths and angles between the joints, the axes of the manipulator were first defined as shown in Figure 5-5, which then helped in creating the DH Table for further analysis. For the prismatic joint, the z-axis was defined along the displacement, while for all the revolute joints, the z-axis were defined out of the plane. Moreover, for the x-axis, the direction perpendicular to any of the consecutive z-axes was selected as the x-axis.

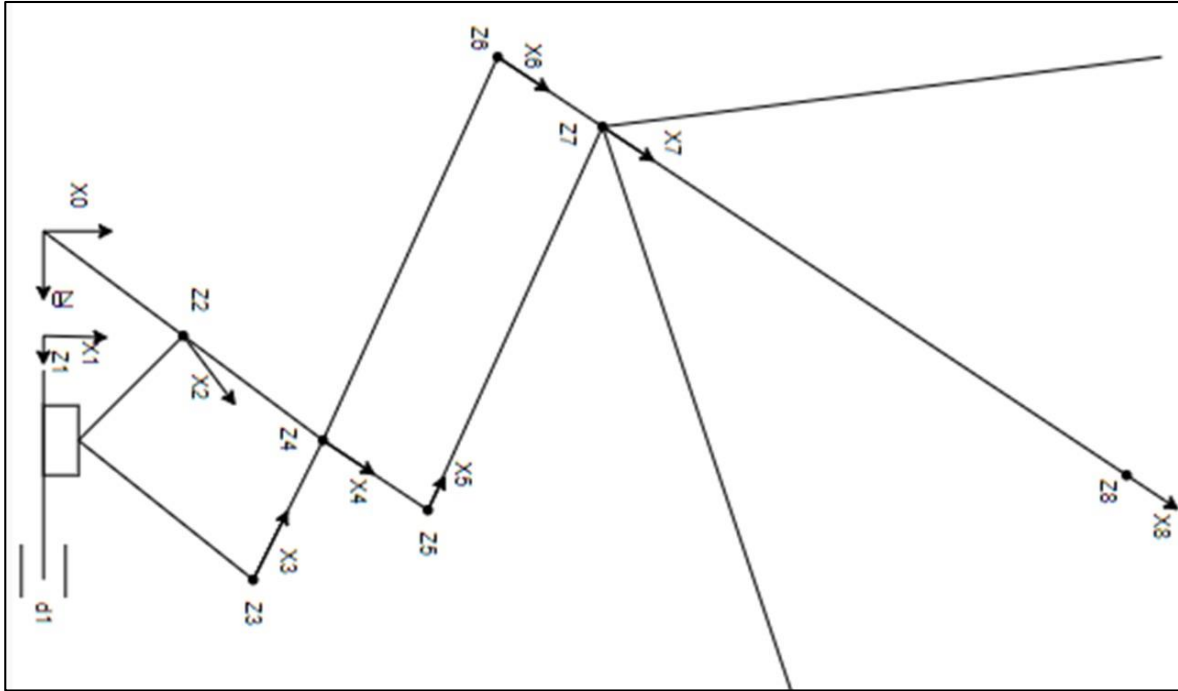


Figure 5- 5: Axes Placement

After determining the parameters of the DH table, the transformation matrices were constructed, and the final transformation matrix 0_8T was worked out, using the generalized transformation matrix shown in equation. This final transformation matrix is then used to transform the cartesian coordinates of the end-effector in to the inertial reference frame.

$${}^{i-1}_iT = \begin{bmatrix} c\theta_i & -s\theta_i & 0 & a_{i-1} \\ s\theta_i c\alpha_{i-1} & c\theta_i c\alpha_{i-1} & -s\alpha_{i-1} & -s\alpha_{i-1}d_i \\ s\theta_i s\alpha_{i-1} & c\theta_i s\alpha_{i-1} & c\alpha_{i-1} & c\alpha_{i-1}d_i \\ 0 & 0 & 0 & 1 \end{bmatrix} = \begin{bmatrix} {}^{i-1}_iR & {}^{i-1}_ip_{iORG} \\ \underline{0} & 1 \end{bmatrix}$$

Once the transformation matrices have been determined, the 2-D model of the manipulator is designed on MATLAB and its home position and final position is determined by inputting the desired joint angles equations. These equations are a function of time, which means the joint velocities and acceleration will change during the flight of the robot, and hence there would be a variation in the cyclic loads in during the downstroke and upstroke motions. Figure 5-6 shows the initial and final position of the manipulator in the task space.

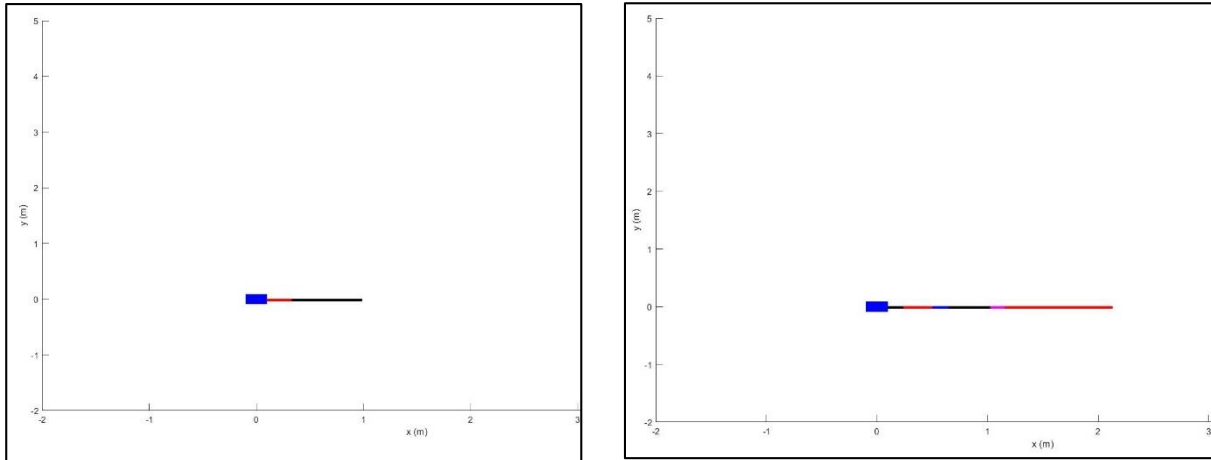


Figure 5- 6: Initial (left) and Final (right) Position

The MATLAB code for determining the transformation matrices and the cartesian coordinates of the end-effector is shown in Appendix B. However, in order to visualize the range of reachable workspace of the manipulator, the translational parameters have been listed down in Table 5-4.

Table 5- 4: Translational Parameters

Home Position (m)			Final Position (m)		
x	y	z	x	y	z
0.9868	-0.0150	-2.4871	2.1303	-0.0115	-1.7805

5.2.3 Mathematical Modeling for Flapping

As a brushless DC motor is being used for the flapping, the modelling involves an electromechanical system as shown in Figure 5-7. Thus, controlling the speed of the motor, will help us directly controlling the flapping frequency, because, the time it takes for a motor to make one complete rotation, is same as the time the wings will take to make a complete stroke.

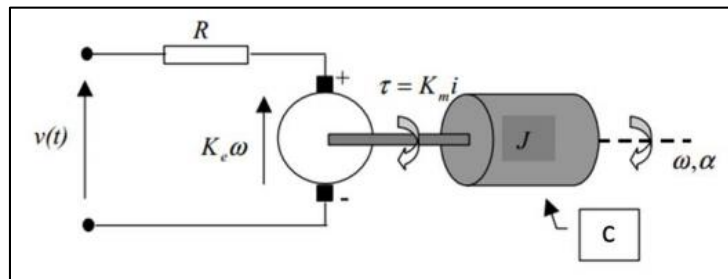


Figure 5- 7: Electro-mechanical model of motor

The electrical and mechanical modelling involved in controlling the flapping frequency, has been shown below.

Electrical Modelling

By using the Kirchhoff's Voltage Law, the electrical circuit can be modelled as,

$$V(t) = L \frac{di}{dt} + Ri(t) + V_b(t) \quad (5.1)$$

where,

$v(t)$ = input voltage (volts)

$i(t)$ = armature current (amperes)

R = resistance of the armature winding, (ohm)

V_b = Back EMF (volts) of motor and is proportional to speed (ω) of rotor, $V_b(t) = K_e \omega(t)$

K_e = back emf constant (V-s/rad)

Assuming the value of inductance to be comparatively less, the above equation can be re-written as:

$$v(t) = R i(t) + V_b(t) \quad (5.2)$$

Mechanical Modelling

$$\Sigma \tau(t) = J\dot{\omega}(t) \quad (5.3)$$

$$J\dot{\omega}(t) = \tau_m(t) - c\omega(t) \quad (5.4)$$

where,

$\omega(t)$ = angular velocity of the rotor, (rad/sec)

J = polar moment of inertia of the moving parts, (Kgm^2)

c = damping coefficient due to the viscous friction, ($N s/m$)

$\tau_m(t)$ = Electro-mechanical torque (Nm) and is proportional to armature current $i(t)$

$$\tau_m(t) = K_m i(t)$$

where K_m = motor constant (Nm/A)

Substituting this value of τ_m in the mechanical model,

$$J\dot{\omega}(t) = K_m i(t) - c\omega(t) \quad (5.5)$$

Solving Equation 5.3 and Equation 5.4 for $\omega(t)$ by putting value of $i(t)$:

$$\frac{RJ}{cR + K_e K_m} \dot{\omega}(t) = -\omega(t) + \frac{K_m}{cR + K_e K_m} \quad (5.6)$$

where

$$T_s = \frac{RJ}{cR + K_e K_m}$$

$$K_{sm} = \frac{K_m}{cR + K_e K_m}$$

Equation 5.6 can be written now as,

$$T_s \dot{\omega}(t) = -\omega(t) + K_{sm} v(t) \quad (5.7)$$

Equation 5.7 is the first order differential equation, whose solution can be found by multiplying by velocity of DC motor.

As the signal would be PWM, hence we assume the dimensionless control signal as the scaled input voltage.

$$u(t) = \frac{v(t)}{V_{\max}} \quad (5.8)$$

Also,

$$K_s = V_{\max} K_{sm} \quad (5.9)$$

$$T_s \dot{\omega}(t) + \omega(t) = K_s u(t) \quad (5.10)$$

Rendering to Laplace domain and transforming Equation 5.10 to transfer function form, we get:

$$G(s) = \frac{\omega(s)}{u(s)} = \frac{K_s}{T_s s + 1} \quad (5.11)$$

Putting value of $K_s=186 \text{ rad/sec}$, $T_s=1.04 \text{ sec}$

$$G(s) = \frac{186}{1.04s + 1} \quad (5.12)$$

PID Controller Design

After completing the mathematical modeling, the close-loop transfer function was built on MATLAB (Simulink). The actuator transfer function and the sensor transfer function were assumed to be 1, while for the controller, PID was auto tuned on Simulink to get the desired constants of proportional, derivate, and integral controllers. Figure 5-8 shows the block diagram of the closed loop transfer function, where the plant function being Equation 5.12.

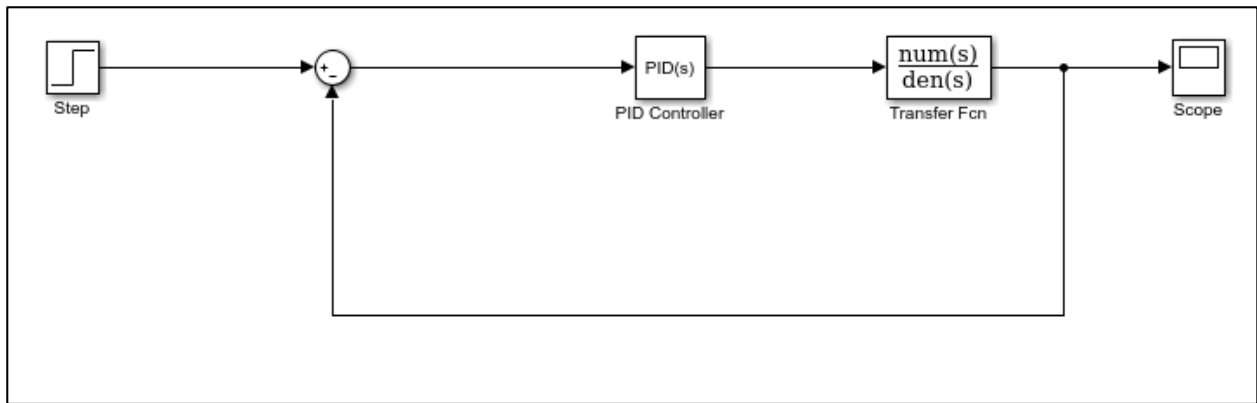


Figure 5- 8: PID Control Loop

Now, the auto-tuning of the transfer function was performed for a step input of 1, and the resulting response has been shown in Figure 5-9.

As it can be seen from the figure, that the transient response of the controller is more robust and the response time is faster. Therefore, during a micro-UAV flight such as that of a Bat, where the need is surveillance of disaster management areas, PID controller which is more robust and faster, is required. For a step input given, the response settles at 1.14 seconds, and the overshoot is 8.63%. A summary of the PID controller constants and the response characteristics is shown in the table.

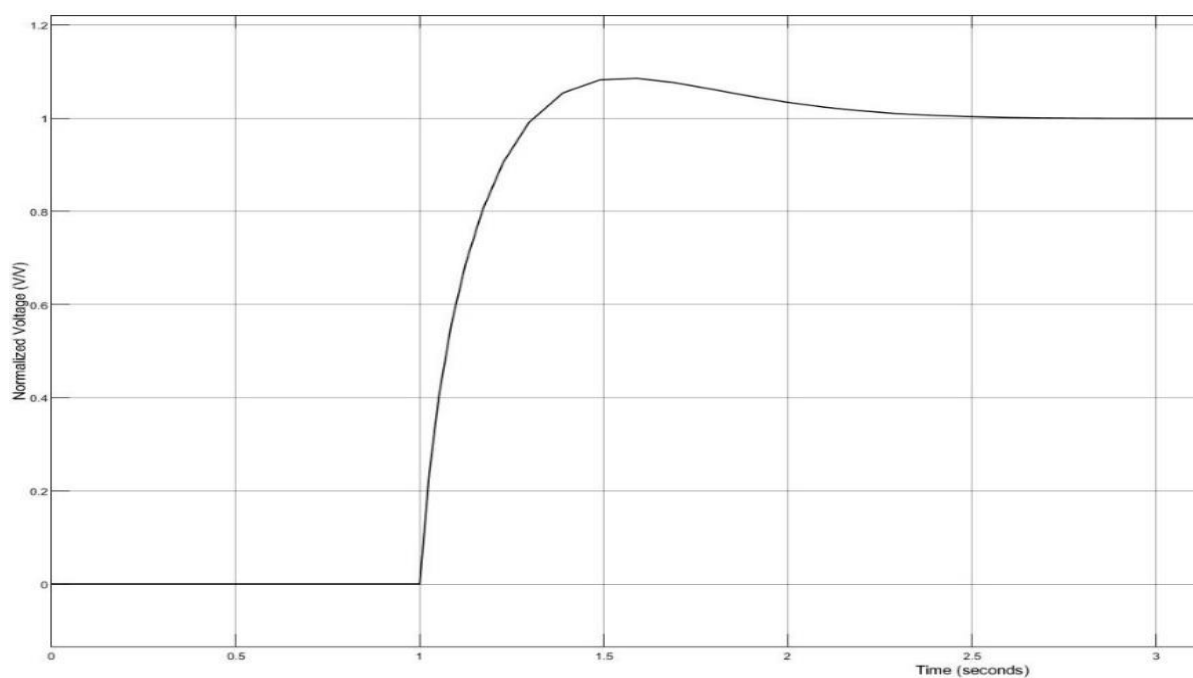


Figure 5- 9: Autotune Response

Table 5- 5: CL System Response Characteristics

Closed-Loop System Response Characteristics	
Proportional (P)	0.0430
Integral (I)	0.1207
Derivative (D)	0.0009
Filter Coefficient (N)	22.184
Rise Time	0.214
Settling Time	1.14
Overshoot	8.63%
Peak	1.09
Closed-loop Stability	Stable

Finally, a closed-feed back controller for the flapping motion of the robot has been designed, which will help the robot to change its flapping frequency based on the reference normalized voltage input given to the motor.

5.2.4 Pulse Width Modulation Signal Generation

In order to provide the voltage to the motor, in the form of Pulse Width Modulation (PWM), a ladder logic diagram was drawn on the TLP LogixPro Simulator® software. This signal will help in controlling the speed of the motor, by varying the input voltage assigned to the High bit. The following components were used to build the ladder logic:

1. Input (open contact)
2. Output
3. NOT Gate (closed contact)
4. On-Delay Timer
5. Off-Delay Timer
6. Count Up
7. Retentive Timer On
8. Divide

The inputs to the timers were associated with the output of the Timer Done (DN) bit rung for the timers, thus the output of one timer is the input of the other. Furthermore, a NOT gate was also introduced into the diagram at the input of the Off-Delay Timer this served to energize the output of this timer when the input of our timer turns off. All of these contacts and components are shown in Figure 5-10.



Figure 5- 10: Initial Ladder Logic Diagram

For illustrative purposes it was decided to choose a duty cycle of 75% which meant that the output will remain in an 'ON' state for 75% percent of the total time. So, the team chose a total time of 0.1 seconds, thereby, the 'ON' state will be 0.075 seconds and the 'OFF' will be 0.025 seconds. It is to noted that the desired frequency is 10 Hz, therefore, the desired frequency has

been achieved by adjusting the time base and timers' values. The on and off timers have a preset time for 0.25 seconds and 0.75 seconds respectively and are in compliance with the time base units of 0.1.

$$Preset = 0.075 \div 0.1 = 0.75 \text{ seconds} \mid Preset = 0.025 \div 0.1 = 0.25 \text{ seconds}$$

Also, it is important to note that the output contact **O:2/4** represents the total time so it will be on for 100% of the time i.e., 0.1 seconds. Whereas **O:2/1** represents the switch that will be turned on for 75% of the time i.e., 0.075 seconds. It can be observed that for the time period of 0.025 seconds the output of the On-Delay Timer, O:2/1, is turned OFF due to the 'delay' in action. So, the Closed Contact at Rung 002 inverts the input signal of OFF from O:2/1 (NOT Gate) to ON and thus the output of the Off-Delay Timer, O:2/4, remains ON.

The final findings for the time of less than 0.025 seconds are summarized in the Table 5-6.

Table 5- 6: Position and State Findings for $t < 0.025s$

Component	Position	State
O:2/4	Input to TON	ON
O:2/1	Output of TON	OFF
O:2/1	Input to TOF	ON
O:2/4	Output to TOF	ON

For the rest of the total time period remaining (0.075 seconds) the output of the On-Delay Timer, O:2/1, is turned ON as the delay/preset value to turn on the output at the Timer Down Bit has been achieved. The Closed Contact at Rung 002 inverts the input signal of ON from O:2/1 (NOT Gate) to OFF. Now as the Off-Delay Timer has now turned 'off' the delay to turn OFF the output will now take place for 0.075 seconds, as specified in figure above; therefore, the output of the Off-Delay Timer, O:2/4, remains ON and this will continue in a loop. The findings after 0.025 seconds are specified in Table 5-7 below.

Table 5- 7: Position and State Finding for $t > 2.5s$

Component	Position	State
O:2/4	Input to TON	ON
O:2/1	Output of TON	ON
O:2/1	Input to TOF	OFF
O:2/4	Output to TOF	ON

Consequently, the output at O:2/4 will remain ON for 100% of the time meanwhile O:2/1 only remains ON for the preset value specified to the Off-Delay Timer. In our case the total time was 0.1 seconds which equated to 1 second in the units specified for the Timer Base of our timers. i.e., the sum of Preset Values for TOF (0.75 seconds) and TON (0.25 seconds) equals 1 second.

Flapping Frequency Calculation

To calculate the time period of the produced waveforms, three more components were added along with their respective inputs/outputs. These were:

1. Counter Up
2. Retentive Timer On
3. Divide

We shall first include the Count Up or CTU that acts as a counter and ‘counts’ the number of low to high states until the accumulated value reaches the set preset value. We set the number of cycles for the circuit to re-run as hundred; therefore, the **preset** value for the CTU above is set to ‘100’. Some modifications were made into the existing diagram such that a closed contact (NOT Gate) associated with the Timer Done Bit of CTU was placed on Rung 0 which serves to break the circuit after all 100 cycles have been completed i.e., CTU Accum value reaches Preset. Similarly, the input at Rung 4 to CTU is the Enable Bit of the Off Delay Timer which turns ‘ON’ every cycle when the On Delay Timer is turned on.

Therefore, once a cycle has been complete - marked by the completion of the Off-Delay Timer reaching 0.075 seconds - the T4:1/EN input contact is energized and the Accum value rises until it's value reaches the Preset of 100. The output of the configuration is shown in the figure below, which shows how the CTU Accum value increases every cycle; every time the Preset value of the Off-Delay Timer is reached the CTU is energized by the Off-Delay Timer 'Enable Bit' - this marks the completion of 1 cycle and therefore increases Accum by 1. Similarly, there is a Closed Contact at Rung 0 'C5:0/DN' which breaks the cycle to completion. Once the CTU Preset value is reached the Timer Done Bit is enabled and the NOT Gate (closed-contact) at C5:0/DN inverses the 'ON' state to 'OFF' which cancels any further count initiated by the on delay and subsequently the off-delay timer, thereby, concluding the process.

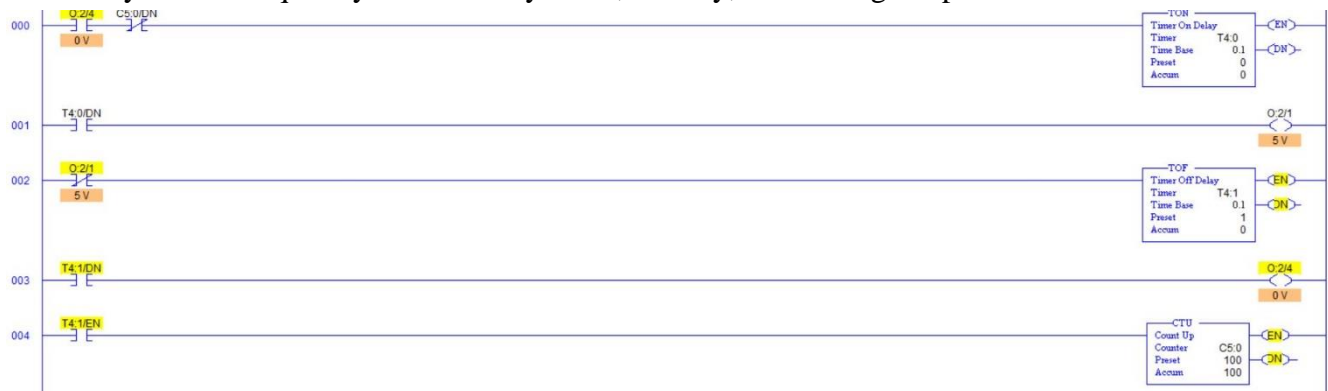


Figure 5- 11: Output Configuration

Now with the number of cycles stored in the Accum Value of the **CTU** we need to calculate the total time taken to complete the 100 cycles. This was found using the Retentive Timer On component which basically counts time base intervals, like other timers, until the preset value is reached. Moreover, a configuration of OR Gate was made using our two outputs from the timers. As mentioned earlier 'C5:0/DN' breaks the circuit once CTU finishes counting. Once C5:0/DN deactivates, the RTO Accum value will stop counting and store it for 100 cycles. It is also worth noting that an arbitrarily large Preset value was employed so that it is not crossed when used for larger cycles.

Finally, two Divide components were used in our last rung that utilized the data obtained from the Counter Up and Retentive Timer On components. These are shown in Figure 5-12.

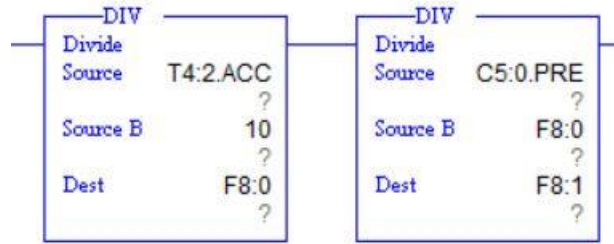


Figure 5- 12: Divide components

The first Divider was used to ‘fix’ the units of the Accumulated Value obtained from the RTO (T4:2.ACC) (because the Time Base Value was 0.1 not 1s.) So,

$$Time = Accumulated \times Time\ Base$$

The Second divide was used to source the information from the counter Up and divide it by the time stored in F8:0 destination (output)

$$Frequency = Number\ of\ Cycles \div Total\ Time$$

$$Frequency = C5:0.PRE \div F8:0$$

This Ultimately gives us the frequency of PWM signal, indicated in Figure 5-13 below, it can be observed that for the total time of 100 seconds, the frequency is 10 Hz.

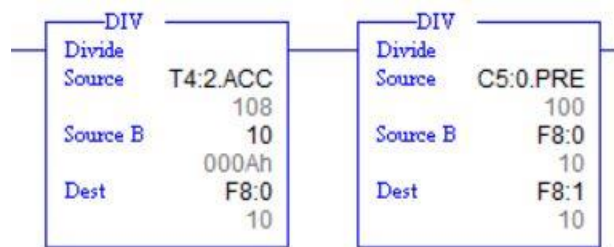


Figure 5- 13: Final Divides

For reference, the final ladder logic diagram is shown in Appendix C. It is to be noted that, the values of timers can be changed in accordance with the desired flapping frequency, but here a time period of 0.1 second has been considered for the simulation purposes.

5.3 Summary

Harvesting energy from moving structures has become a necessity as available sources of electrical energy are very costly and bulky. For light-weight UAVs, the use of batteries adds

unwanted weight to the body, creating problems during flight. Moreover, waste batteries are not decomposable – recycling is not economically feasible and burning releases toxic gases into the atmosphere. Therefore, it was essential to explore alternate sources of energy for the UAV to have a self-sustained light-weight flight so that, if need be, it is able to carry extra payload during disasters.

When the UAV was flapped at a frequency of 2 Hz, piezo-electric transducers attached on the wing-membrane were able to generate an alternating signal of amplitude 60 mV. The signal was then amplified using a non-inverting operational amplifier to achieve 2V output voltage. The results, when compared with previous literature, proved to be reliable and showed that it is possible for the UAV have a self-sustained flight, eliminating the need for an on-board battery.

For optimizing the flapping frequency, the team first derive the mathematical model, and then based on the plant transfer function, a PID controller was deisgn on MATLAB. Hence, a feed-back control for the flapping motion was acheived.

Finally, in order to vary the speed of the motor, a pulse width modulation signal (PWM) was provided to the motor through the programmable logic controller (PLC). In order to vary the frequency and input voltage, a ladder logic diagram was designed on LogixPro software, which was then fed in to the PLC to operate and control the motor.

CHAPTER 6

IMPACT AND ECONOMIC ANALYSIS

6.1 Social Impact

The robot consists of folding and unfolding mechanism which allows it to enter narrow and harmful regions, especially for surveillance during disaster management, that would normally be inaccessible to human and conventional robots. This will help the concerned authorities and NGOs to make use of machines instead of humans to analyze the dangerous zones, and hence reduce the risk to human life. The flapping mechanism which operates at a frequency of 10Hz, allows the robot to achieve maximum flight efficiency, and thus higher lift. Higher flapping frequency enables the robot to cover a larger flight range, thus giving humans the leverage to analyze the disaster affected area from a safe distance. This will not only save their time and effort, but will also allow the authorities to safely communicate with the people present at the site. The use of artificial intelligence can enable robots to make quick decisions in times of crisis, thereby saving precious time that may be otherwise be lost with human operation.

As such, with automation and technology gaining speedy traction, the concerned question arises whether these machines could completely erase the need for human input. However, that would hardly be the case as no machine can match the sheer complexity of the human mind. Therefore, it will be through the unity of man and machine that the most effective solutions to social crises will be formed.

6.2 Sustainability Analysis

6.2.1 Economics of Project

A brief overview of the total project cost breakdown is shown in the bill of materials in Table 6-1 for all the major components of the robot.

Table 6- 1: Bill of Materials

Component	Quantity	Cost / PKR
Carbon Fibre Rods	10	2250
Silicone Membrane	2	28,469
Glass Sheets	3	4300

Aluminium Sheet	1	2400
Test Rig	1	1500
3D Printed Joints	60	1950
Piezoelectric Transducers	10	400
HDMI Cable	1	180
Gears	4	900
BLDC Motor	1	850
ESC with PWM Servo	1	1000
IMU	1	200
Battery	1	1000
	TOTAL	46,859

Based on this information, the construction of such a micro UAV falls well within the limited budgets of conventional rescue facilities. Considering the fact that one robot is designed to last several years, with rechargeable battery, sustainable renewable power source and biodegradable membrane as well, with minimal maintenance, the economic impact of even one unit is far less than the advantage gained from it.

6.2.2 Scope of Implementation

Since the robot is designed to be light, robust and highly maneuverable, the scope of its operation may be limitless. The temperature range of operation ranges from -50 C to +200 C, which is well within regular climate ranges. The presence of carbon fibre and silicon membrane allow it to operate in humid conditions as they will not rust and the aluminium joints are also resistant to moisture. The electronics are housed within the sturdy depron and hence insulated from external factors. Therefore, geographically speaking, there is minimal hinderance in operation.

The materials and components used in the project have been locally sourced through national vendors, except for the silicon membrane which was imported from the US through Ali Express. However, it is also available without import restrictions.

6.3 Environmental Impact

As the structure of the robot is made from carbon fiber, the weight is significantly low as compare to other machines, like drones. The light weight allows the machine to achieve maximum lift with minimal energy input, thus conserving energy and reducing the burden on environment. Moreover, the machine incorporates piezo electric transducers underneath its membrane, which continuously harvest energy during the flight. This harvested energy can be utilized to operate small sensors and LEDs, thus reducing the burden on the batteries, providing an alternate source of renewable energy. Lastly, the prime mover in the micro-UAV is a brushless DC (BLDC) motor, which means there is no emission of harmful gases, and thus no contribution to greenhouse effect, as is the case with a combustion engine.

6.4 Sustainable Development Goals

Table 6-2 outlines the SDG Mapping for our proposed FYP model.

Table 6- 2: SDG Mapping

S. No	SDG	Adherence of FYP to SDG
1.	No Poverty	
2.	Zero Hunger	
3.	Good Health and Well-Being	The proposed model will be aimed towards acting as a surrogate for human rescue workers in dangerous environments.
4.	Quality Education	
5.	Gender Equality	
6.	Clean Water and Sanitation	
7.	Affordable and Clean Energy	The proposed model consists of a cheap renewable energy source in the form of PZTs.
8.	Decent Work and Economic Growth	
9.	Industry, Innovation and Infrastructure	The successful implementation of this project will pave the way for further research in bio-inspired robotics.
10.	Reduced Inequalities	

11.	Sustainable Cities and Communities	The proposed model consists of a cheap renewable energy source in the form of PZTs.
12.	Responsible Consumption and Production	
13.	Climate Action	
14.	Life Below Water	
15.	Life on Land	
16.	Peace, Justice and Strong Institutions	
17.	Partnerships	The supporting funds from the local government are helpful in aiding the already overburdened rescue groups.

6.5 Hazard Identification and Safety Measures

The major safety hazard that could potentially disrupt operation is the loss of power. This could be caused by the battery draining out or loss of connection within the circuit. For safeguard, the design consists of a backup power source in the form of the energy harvesting subsystem which will provide at least the minimum power for a safe landing.

Other hazards include the sharp edges of the carbon fibre rods, which could potentially pierce the silicon membrane. To ensure safe operation, all rods are blunted and covered with hot glue to restrict chances of piercing.

During the manufacturing process of the membrane, safety equipment was used to handle the liquids and only appropriate materials were used for moulding and curing the membrane.

All electronics are operated within operational standard and recommended conditions.

6.6 Summary

The most important social aspect of the project is that the robot consists of folding and unfolding mechanism which allows it to enter narrow and harmful regions, especially for surveillance during disaster management, that would normally be inaccessible to human and conventional robots. And as far as economics is concerned, the construction of such a micro-UAV falls well within the limited budgets of conventional rescue facilities. Moreover, the structure of the robot is made from carbon fiber, the weight is significantly low as compare to other machines, like drones. The light weight allows the machine to achieve maximum lift with minimal energy input, thus conserving energy and reducing the burden on environment. However, the major safety hazard that could potentially disrupt operation is the loss of power. This could be caused by the battery draining out or loss of connection within the circuit.

CHAPTER 7

CONCLUSION AND FUTURE RECOMMENDATIONS

7.1 Conclusions

The project aimed at the design and development of a biologically inspired flying machine having bat morphology for disaster management. The objectives included simulating the design using modern computational tools, autonomously executing a point-to-point flight and to test the machine under various simulated conditions of disaster. Moreover, one of the main objectives was to harvest energy from the flapping motion of the robot by converting the cyclical stress in to electrical signals via piezo-electric transducers.

After an extensive brainstorming, a concept was finalized to achieve the key degrees of actuation (DOA) for the robot, which included the forelimb flapping motion, forelimb mediolateral motion, and hindlimb dorsoventral motion. For the forelimbs, Watts six bar linkage was utilized, while for the flapping, a simple crank-shaft mechanism was selected.

Proceeding towards the embodiment design phase, the aerodynamic and geometric parameters of the UAV were calculated and the inverse and forward kinematic analysis of the linkages was performed on MSC Adams in order to determine the required motor for actuation. In addition to the inverse kinematic analysis, the trajectory planning of the robot was also performed using a systematic approach. First the Denavit Hartenberg (DH) table was constructed, through which the transformation matrices of the manipulator were worked out. Using the transformation matrices, the reachable and dexterous workspaces of the robot were determined. Moreover, a complete 3-D model of the robot was designed on SolidWorks through which the detailed drawings were used for manufacturing and assembling of the parts. Making use of the detailed design, the fabrication process was started, in which first the silicon membrane was manufactured using the glass sheets pressing method. The links for the Watts six bar chain were cut from carbon fiber rods, while the joints of the linkage were wire cut using aluminum. For the flapping motion, the links were made from traditional machining of aluminum and were coupled with the forelimbs to perform flapping and folding simultaneously. Finally, the spindle drives were connected to the forelimbs via a bearing coupled with an aluminum disc, and the motors were connected for actuating the mechanism.

After completing the assembly, the membrane was attached on the wing structure and piezo-electric transducers were placed beneath the membrane for harvesting energy.

Finally, the testing of the robot was performed, in which the flapping frequency was kept at 2 Hz. An oscilloscope was connected to the piezo-electric transducers, which showed a sinusoidal wave pattern on the screen once flapping was initiated. A root mean square (RMS) value of 60mV was obtained. Hence, one of the main objectives of harvesting energy and reducing our dependence on batteries to power small sensors was achieved in the project. However, most of the sensors work in the range of 2-5 V, therefore, the signal generated through flapping was amplified using an amplification circuit on MATLAB. To conclude, the amplified signal had a peak value of about 2 V, and hence, the piezo-electric transducer coupled with the amplification signal was now capable of powering small sensors such as infrared, proximity, and temperature sensors during disaster management.

For optimizing the flapping frequency, the team first derive the mathematical model, and then based on the plant transfer function, a PID controller was deisgn on MATLAB. Hence, a feed-back control for the flapping motion was acheived.

Finally, in order to vary the speed of the motor, a pulse width modulation signal (PWM) was provided to the motor through the programmable logic controller (PLC). In order to vary the frequency and input voltage, a ladder logic diagram was designed on LogixPro software, which was then fed in to the PLC to operate and control the motor.

7.2 Future Recommendations

The use of new and improved materials with priority of having less weight is the top most future development for this project. The use of aluminum joints have resulted in increased weight of the overall robot, therefore, there is room for further reduction in the weight. Furthermore, the usage of light weight electronics can play an important role in the overall weight reduction. Over the last few years a swift development has been observed in the field autonomous flights. To obtain enhanced results from the robot, autonomous point to point path generation can be incorporated. With appropriate path tracker and speed tracker, the robot can cover up the desired distance autonomously. It can be programmed with various alternative responses in order to tackle the situation that it might meet in flight. However, the additional electronics that would be used for this purpose must also be light weight. Moreover, multiple

sensors can be used in this robot for better obstacle navigation. These includes proximity sensors, infrared sensors, temperature sensors, etc. This will give real tie knowledge of the atmosphere and the robot can be programmed to maneuver accordingly.

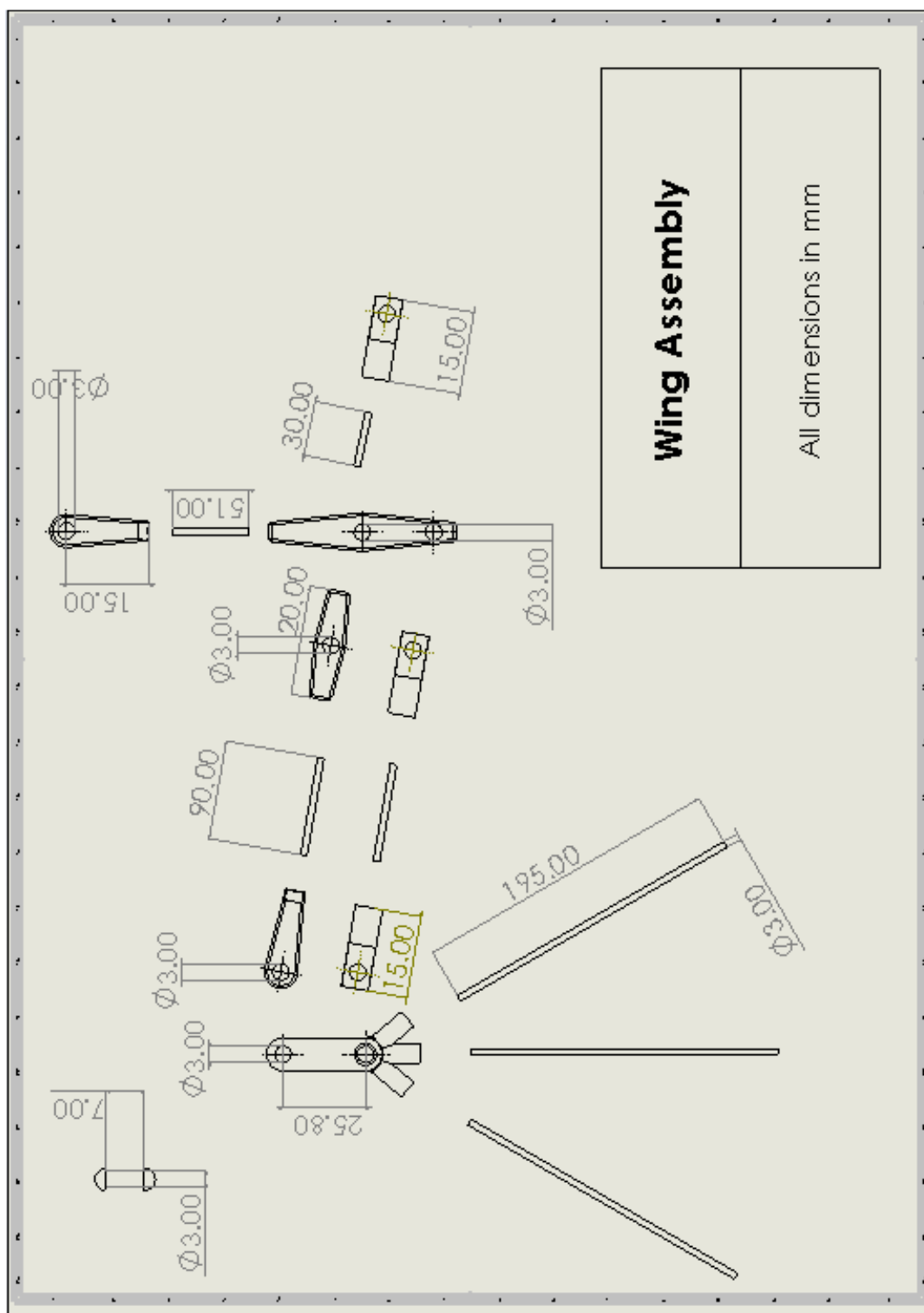
References

- [1] R. R. Murphy, Disaster Robotics, Massachusetts Institute of Technology, 2014.
- [2] D. E. Alexander, Nature's Flyers: Birds, Insects, and the Biomechanics of Flight, John Hopkins University Press, 2002.
- [3] A. Ramezani, X. Shi, S.-J. Chung and S. Hutchinson, "Bat Bot (B2), A Biologically Inspired Flying Machine," IEEE, 2016.
- [4] A. A. Paranjape, S.-J. Chung and J. Kim, "Novel Dihedral-Based Control of Flapping-Wing Aircraft With Application to Perching," IEEE, 2013.
- [5] J. D. Colorado, "BaTBoT: a biologically inspired flapping and morphing bat robot actuated by SMA-based artificial muscles," Universidad Politecnica de Madrid, Madrid, Spain, 2012.
- [6] D. K. Riskin, D. J. Willis, J. Iriarte-Diaz, T. L. Hendrick, M. Kostandov, J. Chen, D. H. Laidlaw, S. K. Breuer and S. M. Swartz, "Quantifying the complexity of bat wing kinematics," *Journal of Theoretical Biology*, vol. 254, no. 3, pp. 604-615, 2008.
- [7] A. Hedestrom, L. Johansson, M. Wolf, R. Von Busse, Y. Winter and G. Spedding, "Bat flight generates complex aerodynamic tracks," *Science*, vol. 316, no. 5826, pp. 894-897, 2007.
- [8] R. D. Bullen and N. L. McKenzie, "Scaling bat wingbeat frequency and amplitude," *The Journal of Experimental Biology*, vol. 205, pp. 2615-2626, 2002.
- [9] R. L. Hadimani, J. M. Barandiaran and A. A. El Gendy, Magnetic Nanostructured Materials: From Lab to Fab, Micro and Nano Technologies, 2018.
- [10] J. A. Kilner and P. P. Edwards, Functional Materials for Sustainable Energy Applications, Woodhead Publishing Series in Energy, 2012.
- [11] X. Wang, Frequency Analysis of Vibration Energy Harvesting Systems, Academic Press, 2016.
- [12] J. F. Holler, D. A. Skoog and S. R. Crouch, Principles of Instrumental Analysis, Cengage Learning, 1997.

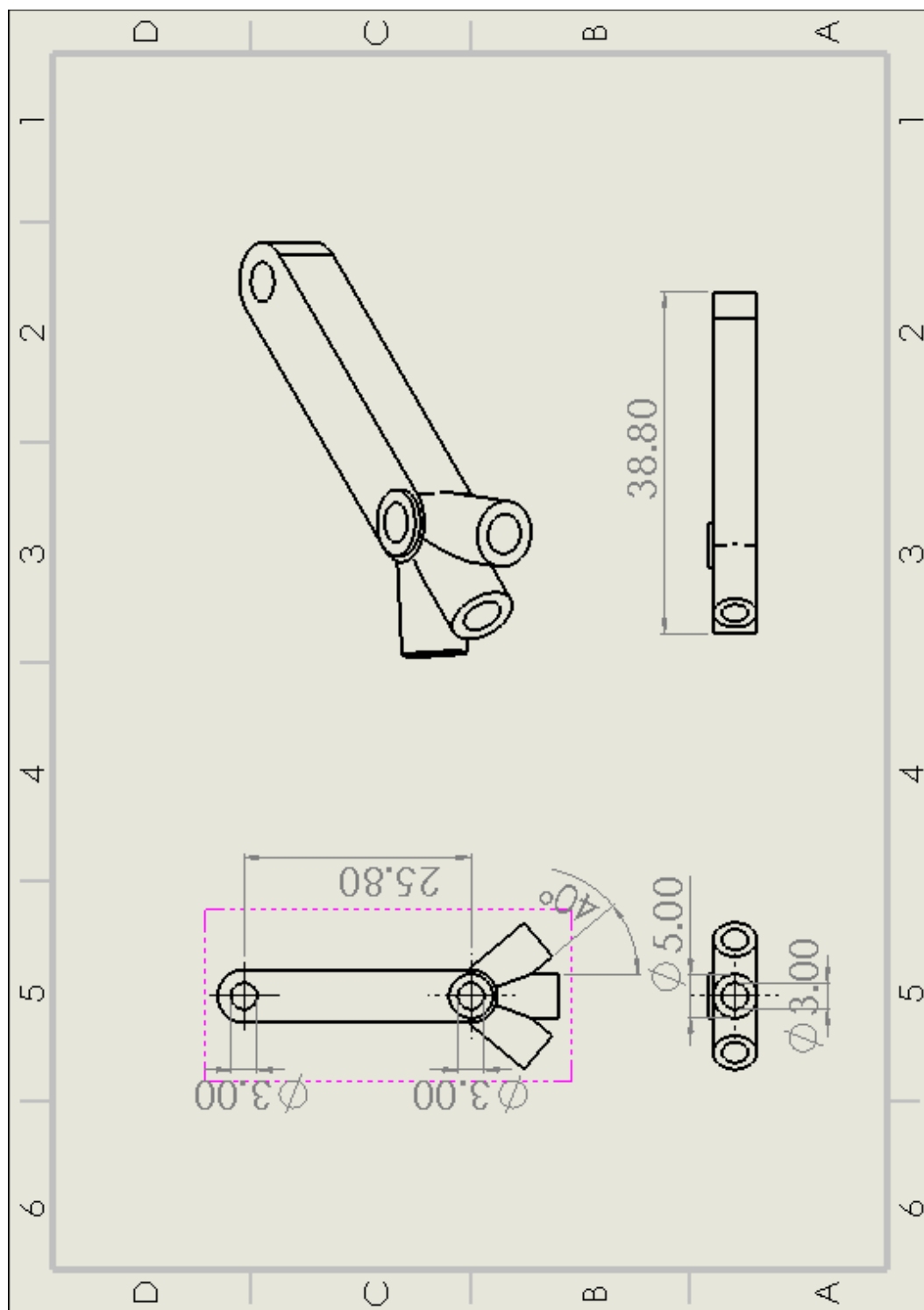
- [13] M. Ericka, D. Vasic, F. Costa, G. Poulin and S. Tliba, "Energy harvesting from vibration using a piezoelectric membrane," *J. Phys IV France*, vol. 128, pp. 187-193, 2005.
- [14] N. M. White, P. Glynn-Jones and S. P. Beeby, "A novel thick-film piezoelectric micro-generator," *Smart Materials and Structures*, vol. 10, no. 4, pp. 850-852, 2001.
- [15] Smooth-On, "Dragon Skin 10 Medium," [Online]. Available: <https://www.smooth-on.com/products/dragon-skin-10-medium/>. [Accessed 4th December 2020].
- [16] D. K. Riskin, J. Iriarte-Diaz, K. M. Middleton, K. S. Breuer and S. M. Swartz, "The effect of body size on the wing movements of pteropodid bats, with insights into thrust and lift production," *The Journal of Experimental Biology*, vol. 213, pp. 4110-4122, 2010.
- [17] R. L. Norton, Design of Machinery, McGraw-Hill, 1999.
- [18] R. G. Budynas and J. K. Nisbett, Shigley's Mechanical Engineering Design, New York: McGraw-Hill, 2011.
- [19] A. Ramezani, X. Shi, S.-J. Chung and S. Hutchinson, "Lagrangian Modelling and Flight Control of Articulated-Winged Bat Robot," in *International Conference on Intelligent Robots and Systems*, Hamburg, 2015.

Appendix A

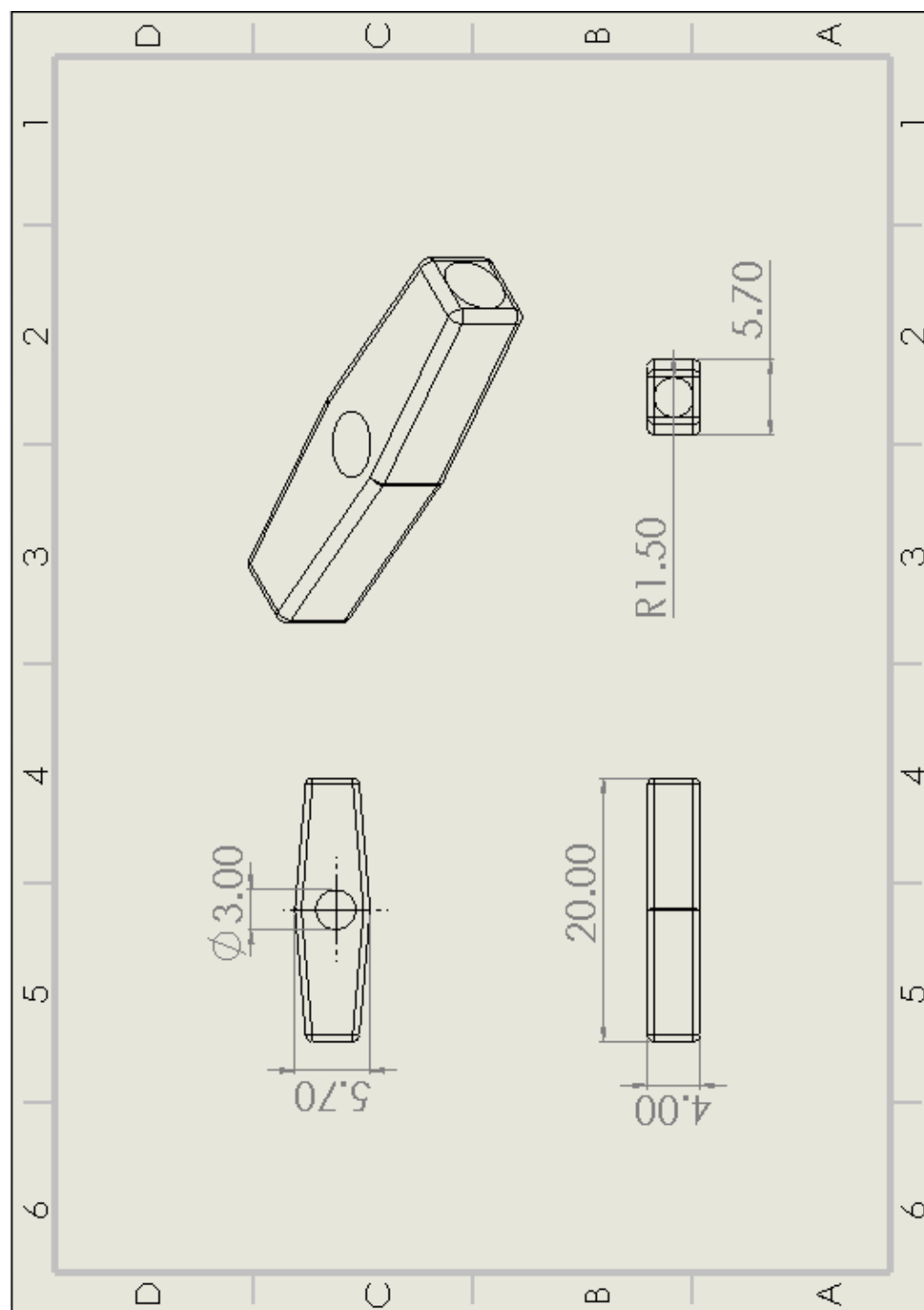
Wing Assembly:

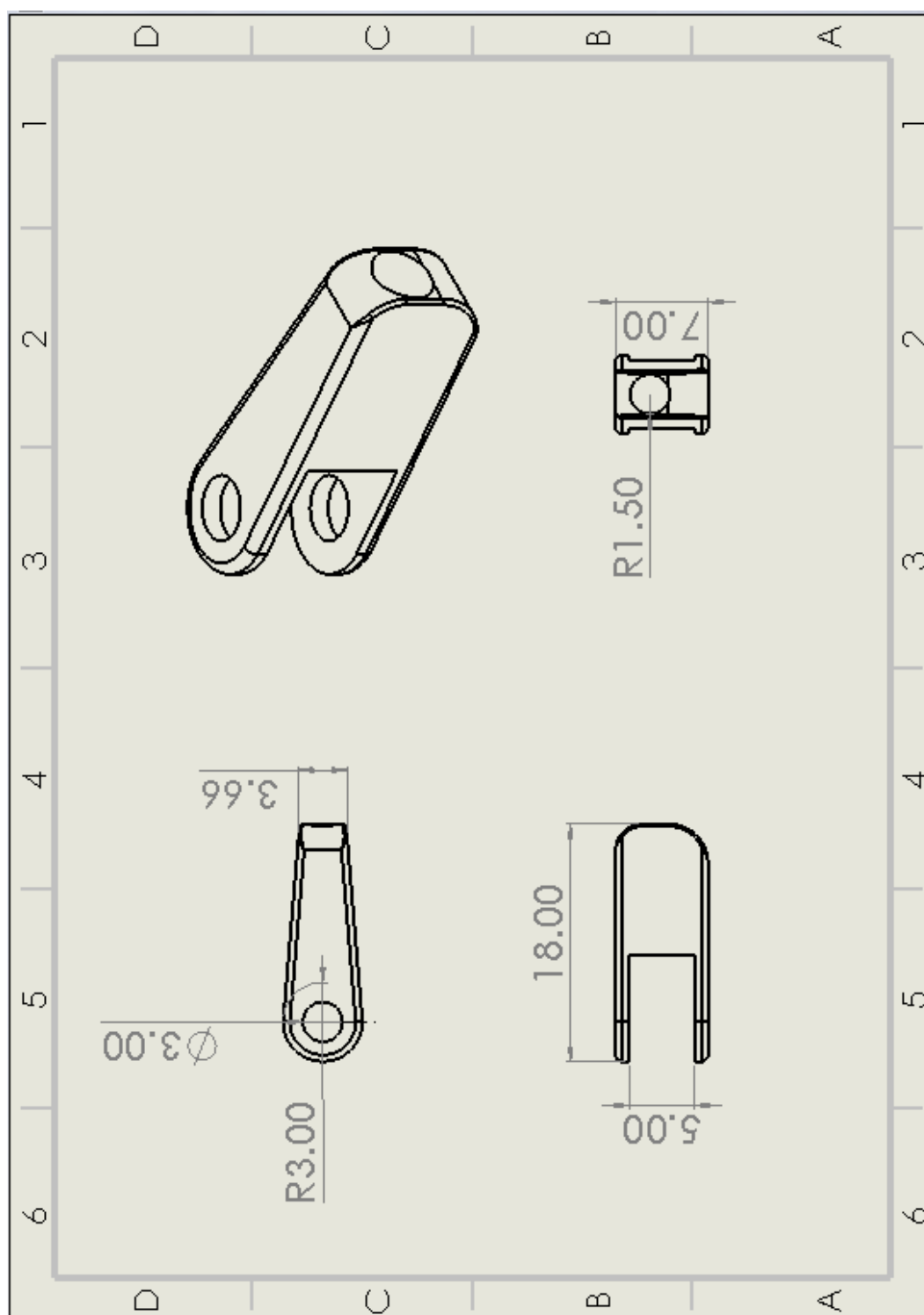


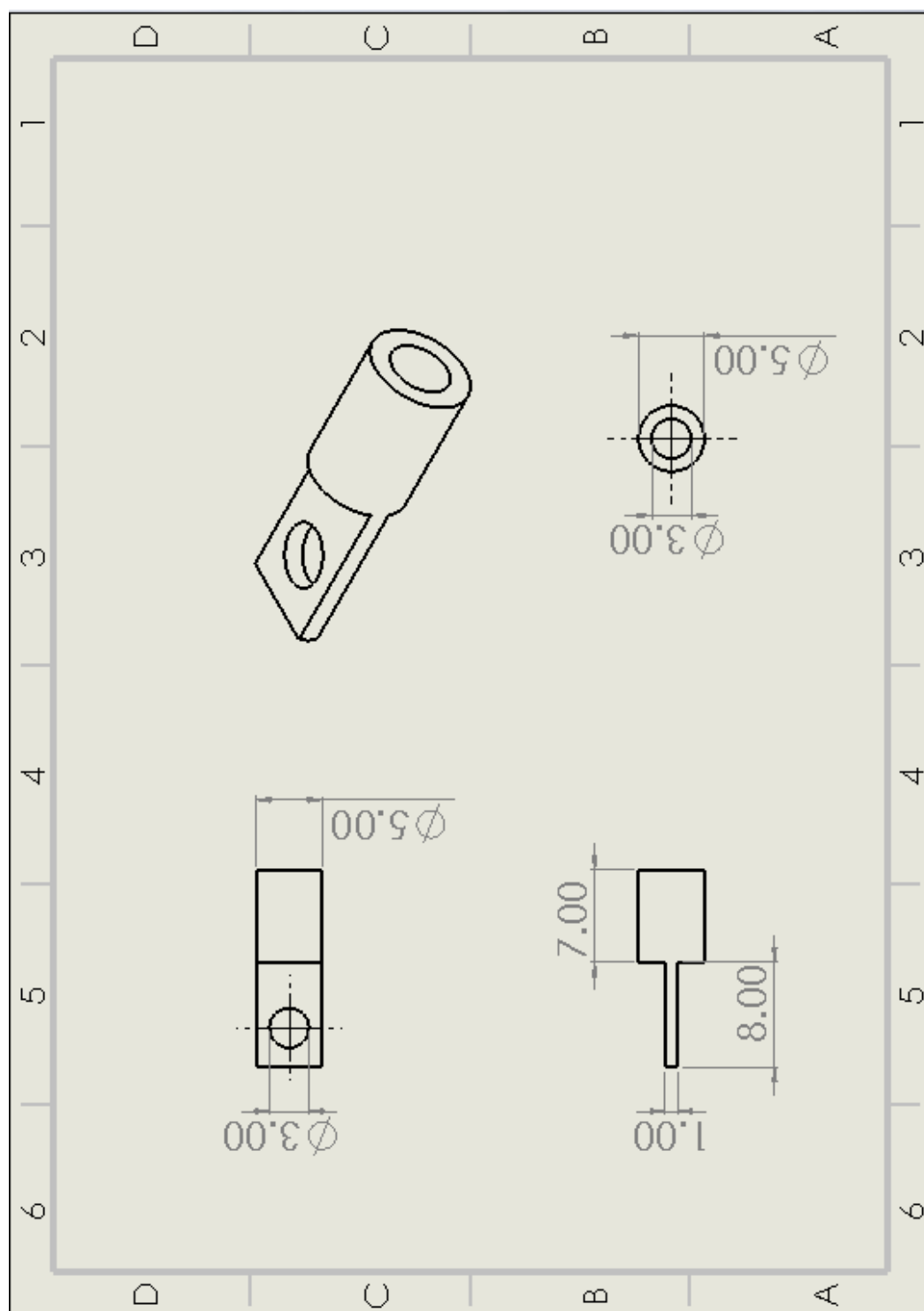
Wrist:



Elbow:



Auxiliary Wrist/Shoulder:

Auxiliary Wrist:

APPENDIX B

MATLAB Code:

```

clc
clear all
format short
q1=0;q2=4*pi/3;q3=2*pi/3;q4=3*pi/2;q5=2*pi/3;q6=4*pi/3;q7=0;q8=0;d1=0.015;
L2=0.240;L3=0.421;L4=0.300;L5=0.294;L6=0.759;L7=0.258;L8=1.950;
q=q1;alpha=pi/2;a=0;d=d1;
T01=[cos(q) -sin(q) 0 a;sin(q)*cos(alpha) cos(q)*cos(alpha) -sin(alpha) -
sin(alpha)*d;sin(q)*sin(alpha) cos(q)*sin(alpha) cos(alpha) cos(alpha)*d;0
0 0 1];
q=q2;alpha=0;a=L2;d=0;
T12=[cos(q) -sin(q) 0 a;sin(q)*cos(alpha) cos(q)*cos(alpha) -sin(alpha) -
sin(alpha)*d;sin(q)*sin(alpha) cos(q)*sin(alpha) cos(alpha) cos(alpha)*d;0
0 0 1];
q=q3;alpha=0;a=L3;d=0;
T23=[cos(q) -sin(q) 0 a;sin(q)*cos(alpha) cos(q)*cos(alpha) -sin(alpha) -
sin(alpha)*d;sin(q)*sin(alpha) cos(q)*sin(alpha) cos(alpha) cos(alpha)*d;0
0 0 1];
q=q4;alpha=0;a=L4;d=0;
T34=[cos(q) -sin(q) 0 a;sin(q)*cos(alpha) cos(q)*cos(alpha) -sin(alpha) -
sin(alpha)*d;sin(q)*sin(alpha) cos(q)*sin(alpha) cos(alpha) cos(alpha)*d;0
0 0 1];
q=q5;alpha=0;a=L5;d=0;
T45=[cos(q) -sin(q) 0 a;sin(q)*cos(alpha) cos(q)*cos(alpha) -sin(alpha) -
sin(alpha)*d;sin(q)*sin(alpha) cos(q)*sin(alpha) cos(alpha) cos(alpha)*d;0
0 0 1];
q=q6;alpha=0;a=L6;d=0;;
T56=[cos(q) -sin(q) 0 a;sin(q)*cos(alpha) cos(q)*cos(alpha) -sin(alpha) -
sin(alpha)*d;sin(q)*sin(alpha) cos(q)*sin(alpha) cos(alpha) cos(alpha)*d;0
0 0 1];
q=q7;alpha=0;a=L7;d=0;
T67=[cos(q) -sin(q) 0 a;sin(q)*cos(alpha) cos(q)*cos(alpha) -sin(alpha) -
sin(alpha)*d;sin(q)*sin(alpha) cos(q)*sin(alpha) cos(alpha) cos(alpha)*d;0
0 0 1];
q=q8;alpha=0;a=L8;d=0;
T78=[cos(q) -sin(q) 0 a;sin(q)*cos(alpha) cos(q)*cos(alpha) -sin(alpha) -
sin(alpha)*d;sin(q)*sin(alpha) cos(q)*sin(alpha) cos(alpha) cos(alpha)*d;0
0 0 1];
T02=T01*T12;
T03=T02*T23;
T04=T03*T34;
T05=T04*T45;
T06=T05*T56;
T07=T06*T67;
T08=T07*T78

axis([-2 5 -2 5]);
Ax1 = [T01(1,4),T02(1,4)];
Ay1 = [T01(2,4),T02(2,4)];
Ax2 = [T02(1,4),T03(1,4)];
Ay2 = [T02(2,4),T03(2,4)];
Ax3 = [T03(1,4),T04(1,4)];

```

```

Ay3 = [T03(2,4),T04(2,4)];
Ax4 = [T04(1,4),T05(1,4)];
Ay4 = [T04(2,4),T05(2,4)];
Ax5 = [T05(1,4),T06(1,4)];
Ay5 = [T05(2,4),T06(2,4)];
Ax6 = [T06(1,4),T07(1,4)];
Ay6 = [T06(2,4),T07(2,4)];
Ax7 = [T07(1,4),T08(1,4)];
Ay7 = [T07(2,4),T08(2,4)];
Ax8 = [-.1,.1];
Ay8 = [0,0];

p1 = line(Ax1,Ay1, 'LineWidth',[3], 'Color','k');
p2 = line(Ax2,Ay2, 'LineWidth',[3], 'Color','M');
p3 = line(Ax3,Ay3, 'LineWidth',[3], 'Color','R');
p4 = line(Ax4,Ay4, 'LineWidth',[3], 'Color','B');
p5 = line(Ax5,Ay5, 'LineWidth',[3], 'Color','k');
p6 = line(Ax6,Ay6, 'LineWidth',[3], 'Color','M');
p7 = line(Ax7,Ay7, 'LineWidth',[3], 'Color','R');
p8 = line(Ax8,Ay8, 'LineWidth',[12], 'Color','B');

drawnow
pause ()
for t=0:0.01:1

q1=0;q2=3*pi/2*t;q3=2*pi/3*t;q4=3*pi/2*t;q5=2*pi/3*t;q6=4*pi/3*t;q7=0;q8=0
;d1=0.01+0.0015*t
    q=q1;alpha=pi/2;a=0;d=d1;
    T01=[cos(q) -sin(q) 0 a;sin(q)*cos(alpha) cos(q)*cos(alpha) -
sin(alpha) -sin(alpha)*d;sin(q)*sin(alpha) cos(q)*sin(alpha) cos(alpha)
cos(alpha)*d;0 0 0 1];
    q=q2;alpha=0;a=L2;d=0;
    T12=[cos(q) -sin(q) 0 a;sin(q)*cos(alpha) cos(q)*cos(alpha) -
sin(alpha) -sin(alpha)*d;sin(q)*sin(alpha) cos(q)*sin(alpha) cos(alpha)
cos(alpha)*d;0 0 0 1];
    q=q3;alpha=0;a=L3;d=0;
    T23=[cos(q) -sin(q) 0 a;sin(q)*cos(alpha) cos(q)*cos(alpha) -
sin(alpha) -sin(alpha)*d;sin(q)*sin(alpha) cos(q)*sin(alpha) cos(alpha)
cos(alpha)*d;0 0 0 1];
    q=q4;alpha=0;a=L4;d=0;
    T34=[cos(q) -sin(q) 0 a;sin(q)*cos(alpha) cos(q)*cos(alpha) -
sin(alpha) -sin(alpha)*d;sin(q)*sin(alpha) cos(q)*sin(alpha) cos(alpha)
cos(alpha)*d;0 0 0 1];
    q=q5;alpha=0;a=L5;d=0;
    T45=[cos(q) -sin(q) 0 a;sin(q)*cos(alpha) cos(q)*cos(alpha) -
sin(alpha) -sin(alpha)*d;sin(q)*sin(alpha) cos(q)*sin(alpha) cos(alpha)
cos(alpha)*d;0 0 0 1];
    q=q6;alpha=0;a=L6;d=0;;
    T56=[cos(q) -sin(q) 0 a;sin(q)*cos(alpha) cos(q)*cos(alpha) -
sin(alpha) -sin(alpha)*d;sin(q)*sin(alpha) cos(q)*sin(alpha) cos(alpha)
cos(alpha)*d;0 0 0 1];
    q=q7;alpha=0;a=L7;d=0;
    T67=[cos(q) -sin(q) 0 a;sin(q)*cos(alpha) cos(q)*cos(alpha) -
sin(alpha) -sin(alpha)*d;sin(q)*sin(alpha) cos(q)*sin(alpha) cos(alpha)
cos(alpha)*d;0 0 0 1];

```



```

    q=q8;alpha=0;a=L8;d=0;
    T78=[cos(q) -sin(q) 0 a;sin(q)*cos(alpha) cos(q)*cos(alpha) -
sin(alpha) -sin(alpha)*d;sin(q)*sin(alpha) cos(q)*sin(alpha) cos(alpha)
cos(alpha)*d;0 0 0 1];
    T02=T01*T12;
    T03=T02*T23;
    T04=T03*T34;
    T05=T04*T45;
    T06=T05*T56;
    T07=T06*T67;
    T08=T07*T78

    axis([-2 5 -2 5]);
    Ax1 = [T01(1,4),T02(1,4)];
    Ay1 = [T01(2,4),T02(2,4)];
    Ax2 = [T02(1,4),T03(1,4)];
    Ay2 = [T02(2,4),T03(2,4)];
    Ax3 = [T03(1,4),T04(1,4)];
    Ay3 = [T03(2,4),T04(2,4)];
    Ax4 = [T04(1,4),T05(1,4)];
    Ay4 = [T04(2,4),T05(2,4)];
    Ax5 = [T05(1,4),T06(1,4)];
    Ay5 = [T05(2,4),T06(2,4)];
    Ax6 = [T06(1,4),T07(1,4)];
    Ay6 = [T06(2,4),T07(2,4)];
    Ax7 = [T07(1,4),T08(1,4)];
    Ay7 = [T07(2,4),T08(2,4)];
    Ax8 = [-.1,.1];
    Ay8 = [0,0];

    set(p1,'x', Ax1, 'y',Ay1)
    set(p2,'x', Ax2, 'y',Ay2)
    set(p3,'x', Ax3, 'y',Ay3)
    set(p4,'x', Ax4, 'y',Ay4)
    set(p5,'x', Ax5, 'y',Ay5)
    set(p6,'x', Ax6, 'y',Ay6)
    set(p7,'x', Ax7, 'y',Ay7)
    set(p8,'x', Ax8, 'y',Ay8)
    drawnow
    pause(.01)

end

```

Home Position Transformation Matrix:

T08 =

-0.0000	1.0000	0	0.9868
-0.0000	-0.0000	-1.0000	-0.0150
-1.0000	-0.0000	0.0000	-2.4871
0	0	0	1.0000

Final Position Transformation Matrix

T08 =

0.5000	0.8660	0	2.1303
-0.0000	0.0000	-1.0000	-0.0115
-0.8660	0.5000	0.0000	-1.7805
0	0	0	1.0000

APPENDIX C

